CANADIAN THESES

THÈSES CANADIENNES

NOTICE

The quality of this microfiche is heavily dependent upon the quality of the original thesis submitted for microfilming. Every effort has been made to ensure the highest quality of reproduction possible.

If pages are missing, contact the university which granted the degree.

Some pages may have indistinct print especially if the original pages were typed with a poor typewriter ribbon or if the university sent us an inferior photocopy.

Previously copyrighted materials (journal articles, published tests, etc.) are not filmed.

Reproduction in full or in part of this film is governed by the Canadian Copyright Act, R.S.C. 1970, c. C-30.

AVIS

La qualité de cette microfiche dépend grandement de la qualité de la thèse soumise au microfilmage. Nous avons tout fait pour assurer une qualité supérieure de reproduction.

S'il manque des pages, veuillez communiquer avec l'université qui a conféré le grade.

La qualité d'impression de certaines pages peut laisser à désirer, surtout si les pages originales ont été dactylographiées à l'aide d'un ruban usé ou si l'université nous a fait parvenir une photocopie de qualité inférieure.

Les documents qui font déjà l'objet d'un droit d'auteur (articles de revue, examens publiés, etc.) ne sont pas microfilmés.

La reproduction, même partielle, de ce microfilm est soumise à la Loi canadienne sur le droit d'auteur, SRC 1970, c. C-30.

THIS DISSERTATION
HAS BEEN MICROFILMED
EXACTLY AS RECEIVED

LA THÈSE A ÉTÉ
MICROFILMÉE TELLE QUE
NOUS L'AVONS REÇUE

PEAK POWER-HANDLING CAPACITY OF FINLINE STRUCTURES EVALUATED BY NUMERICAL AND EXPERIMENTAL METHODS

By

WARREN YUE

A Thesis
Presented to the University of Ottawa
in Fulfillment of the Thesis
Requirements for the Degree of
Master of Applied Science
In
The Department of Electrical Engineering
Faculty of Science and Engineering

ISBN 0-315-33261-1

UNIVERSITÉ D'OTTAWA
UNIVERSITY OF OTTAWA

The University of Ottawa requires the signatures of all persons using or photocopying this thesis. Please sign below, and give address and date.

ACKNOWLEDGEMENTS

The author wishes to express his most sincere gratitude to his supervisor, Dr. M.M. NEY, who has made valuable advice and guidance throughout this work.

The author is particularly grateful to Dr. G.I. Costache for his considerable assistance in providing the Finite Element computer program used in this thesis.

Thanks are also due to Dr. W.J.R. Hoefer for his valuable comments and for having provided the Boundary Element Method computer program, used in this thesis. The author is indebted to those who are at the National Research Council,in particular Mr. A. Hendry, for setting up the experiment and his assistance during the measurements. The Author also like to express his appreciation to Dr. J.P. Noad from Communication Research Centre, who provided the excellent SEM micrographs of the finline samples.

Thanks are due to all the staff and colleagues of the Department of Electrical Engineering at the University of Ottawa with whom the author had the pleasure of knowing, particularly, Ms. E. Chan for her suggestions and help throughout this thesis.

Finally, special thanks are given to the parents of the author for their encouragement and support.

ABSTRACT

The electric field breakdown in various E-plane transmission lines is investigated, in the frequency range from 1 to 140 GHz. The influence of frequency, pressure, temperature and inhomogeneity of the applied field on the breakdown field value is discussed. Application to finline structures is presented, and the peak power handling capacity of these lines is determined theoretically, using a convenient quasi-static approach that can be extended to many E-plane structures. The theoretical analysis in this thesis is evaluated by two numerical methods, namely, the Finite Element and the Boundary Element Methods. In order to test the accuracy of both methods, experiments were performed in static operations and at 9.6 GHz. Comparison between experimental results and theoretical prediction are presented.

It is found that the peak power handling capacity of finlines, although much lower than that of the empty waveguide structure, is still much above levels of power that solid-state devices can presently generate in pulsed operation.

CONTENTS

LIST OF TABLES

LIST OF FIGURES

Chapter 1

INTRODUCTION

With the increasing activities in the millimeter-wave field, much attention has been paid to planar transmission media. Among them, E-plane structures may be purely dielectric, purely conducting or a combination of both in the form of fins or strips on a dielectric substrate which is in the E-plane of the dominant mode of an empty rectangular waveguide. More specifically, finlines are inhomogeneous types of transmission media which are frequently used in microwave integrated circuits because of their favorable properties, such as low dispersion, broad single mode bandwidth, moderate attenuation, and compatibility with solid state chip devices.

The present work treats one aspect of the power limitation, namely, the breakdown phenomenon which is the major factor that limits the power for radar pulse signal transmissions. This is determined by the maximum electric field strength that can exist in a given structure. Indeed, for this type of narrow pulse signals, one can legitimately assume that , due to the relatively low average power involved in those cases, dissipations in the dielectric substrate and in the conducting strips are not important. Hence, breakdown in the air or in the dielectric will occur much before any significant heating of the structure, even at high frequencies at which dielectric losses and dissipation in the conductors become important.

A quasi-static approach is proposed to determine the maximum electric field strength value from which the corresponding maximum power, that the line can sustain, is derived. This approach simplifies considerably the numerical procedure as compared to the dynamic approach. In addition, it can be applied to other types of E-plane structures such as coplanar waveguides, slotlines, coplanar striplines etc. Finally, a thorough investigation of the effect of frequency, temperature, inhomogeneous characteristic of applied electric field and pressure on the breakdown electric

field value is proposed. The effects of superimposed DC field that results from the biasing of solid state components as well as DC magnetic field produced by ferrite elements are also discussed.

1.1 Motivations

Most efforts in the millimeter-waves range has been directed towards the determination of the propagation coefficient and characteristic impedance. However, no data on the power handling capacity of transmission media are available, yet it is of great importance regarding their utilization in radar systems. Indeed, there is a trend towards complete integration of receiver/transmitter systems in planar technology. Power-handling capacity has not been a predominant factor, because of the relatively low power that solid state generators can produce. With the recent development of relatively high-power solid state sources at millimeter waves, as reported by Bhartia and Bahl [1], there is a growing concern about the power that the transmission media can sustain.

Moreover, ionization in gas subjected to alternating electric fields differs in several important respects from ionization in steady (d.c.) fields. The major factors for air breakdown are the gas pressure, the mean free path and the frequency, however, no data on how these factors affect the air breakdown at millimeter wave frequencies is available.

Finally, a quasi-static approach allows one to study peak-power handling capacity of a wide variety of planar structures with relatively low computation cost since one deals with two-dimensional problems in this case.

1.2 State of present knowledge

Very little work, theoretical as well as experimental, has been done on the power-handling capacity of transmission lines in the millimeter-wave range, probably be-

cause the potential use of planar technology at relatively high power is quite recent.

A pioneer work was carried out by Hopfer [2] on the power-handling capacity of ridged waveguides with realistic profiles. A quasi-static approach was used, the maximum power was evaluated by considering the electric intensity at the center of the guide being equal to 30 kV per cm, which is the static air-breakdown value. Since the electric field strength at the edges of the ridge is normally much higher than at the center, correction factors were utilised.

More recently, an interesting study on the power limitation for dielectric waveguides was reported [3]. For single HE mode transmission, the limits imposed by dielectric heating and dielectric breakdown were investigated. The approach for dielectric heating was to find the power level that will cause the temperature at the center of the dielectric rod to reach its melting point. One remarkable conclusion was that, theoretically, limitation due to the dissipation in the dielectric would occur before breakdown, for CW signals. This observation is also true in the case of E-plane structures where the CW-power capability is always much lower than the peak-power rating.

From [4], the power-handling capacity of unilateral and bilateral finline has been evaluated using a static approach. Since the edge profile was unknown, semi-circle and double semi-circle edge profiles were assumed. Electric field was computed using Boundary Element Method(BEM), however, the field value near the conducting strips, which was of particular interest in this case, was calculated from the surface charge density distribution, which turned out to have some discrepency with experimental data. Subsequent comparisons with results obtained with Finite Element Method(FEM) confirmed that BEM was not suitable for geometries containing quasi-infinitely thin subregions.

Chapter 2
THEORY

2.1 Introduction

Since one is only interested in the breakdown field value, one has to determine the field configuration of a given structure and seek the maximum field strength. Consider the structures of the finlines shown in Fig. 2.1. The electromagnetic fields are concentrated around the planar structure and one may assume that the maximum field value will be located somewhere in between the fins.

This type of waveguides is highly inhomogeneous and the methods to evaluate the electromagnetic fields are rather involved. In addition, since the fins are generally not insulated from the enclosure, the dominant mode is not Transverse Electromagnetic (TEM). Even if they were insulated, in order to allow biasing of solid state devices, serrations would be made on the conducting strips to suppress the TEM mode, enabling a mono-mode operation at high frequencies. In fact, the dominant mode is even not purely TE or TM but hybrid. In addition, to avoid singularities in the electric field values that arise at the edges of the conducting strips, realistic profiles should be used. Unfortunately, numerical methods such as Spectral Domain (SDM) [6], Hybrid-Mode analysis (HMA) [7], or Transmission Line Matrix (TLM) [8] are difficult to implement for such geometries. In this approach, one shall consider the guide near the dominant mode cutoff, where all higher order modes are greatly attenuated. The dominant mode can be approximated as quasi-static in between the fins, where the maximum electric field strength should appear. This allows one to use a static approach to solve the problem and simplifies considerably the numerical procedure.

Various methods have been proposed to solve electrostatic problems. The most well known are the Finite Element (FEM) [16] and the Boundary Element methods

(BEM) [9][22], they will be described and compared. The FEM uses differential operators whereas the BEM applies an integral equation formulation of the problem. The variational differential equation formulation related to FEM is computationally simpler and requires no extra equation for the interface problem. For BEM, generally smaller systems of equations and considerable reduction in the data is required to run a problem. However, the unknown potential has to be found indirectly subsequent to source distributions which have to be first evaluated.

2.2 Assumptions

Although a quasi-static approach is used for the maximum field strength computation, the corresponding power transmitted through the guide must be determined with other methods that account for the non-static character of the electromagnetic field in the entire structure. In other words, the characteristic impedance of the line, which is frequency dependent, must be evaluated. Then, the power can be determined by the following relation :

$$P_{max} = \frac{V_{max}^2}{2Z_0}, \tag{2.1}$$

where V_{max} is the maximum static voltage corresponding to the maximum static electric field strength permissible before breakdown, and Z_0 is the power-voltage definition of the characteristic impedance of the line. The above relation is approximately valid over the first part of the operating range in the dominant mode for the following reasons :

(i) Analyses of the electric field configuration above cutoff with the SDM shows that electric field components were neglected with respect to the one in the transverse plane parallel to the substrate. Consequently, E_{max} remains approximately at the static value.

(ii) As the frequency increases, the electric field tends to confine itself within the

dielectric in which the breakdown value is about 5 to 10 times larger than in the air, depending on the type utilized.

(iii) The characteristic impedance which is determined by the SDM for infinitely thin conductors, changes only within few percents when their thickness is taken into account [10].

Finally, it can be safely assumed that the realistic profiles of the conducting strips does not change the value of Z_0 significantly.

2.3 Finite Element Method

The FEM, which is based on a variational technique, is algorithmically simple and efficient. The variational method utilizes certain minimizing principles that guarantee stable convergence for assoeiated numerical processes [23]. A functional, which is a mapping from a function space to the real or complex space, (usually proportional to a physical quantity such as energy), is derived from the fundamental equation associated with its boundary conditions, in terms of the unknown function. The variational method finds the unknown function that minimizes the functional.

Consider the following equation

$$\mathrm{L}u = f\,, \tag{2.2}$$

where L is a linear operator associated with boundary conditions, u, the unknown function and f,the enforcing (input) function. It can be shown [16] that the functional associated with (2.2) is given by

$$F = \langle \mathrm{L}u, u\rangle - 2\langle u, f\rangle\,, \tag{2.3}$$

where $\langle\cdot,\cdot\rangle$ indicates inner product in the function space, which is expressed by:

$$\langle u, v\rangle = \int_\Omega uv^*\, d\Omega\,, \tag{2.4}$$

where Ω is the region of interest and $*$ denotes the conjugate. Pictorially, the inner product gives the *component* of the function u in the *direction* of v.

In the case of electrostatic problems, for instance the functional is given by

$$\mathcal{F}(\phi) = \int_\Omega \epsilon(\nabla\phi)^2\, d\Omega\,, \tag{2.5}$$

which corresponds to twice the amount of stored electric energy in the system.

A function u which minimizes the functional (2.3) is a solution of (2.2). If the operator L is self-adjoint and positive-definite, then the solution u is unique. Self-adjointness is required for stationarity of the functional and to prove the minimal

functional theorem, an operator is said to be self-adjoint if the following condition is fulfilled :

$$\langle \mathrm{L}u, v\rangle = \langle u, \mathrm{L}v\rangle\,. \tag{2.6}$$

Self-adjointness of an operator depends upon the associated boundary conditions. To prove the minimal functional theorem, the operator must be positive-definite:

$$\langle \mathrm{L}u, u\rangle \begin{cases} > 0; & u \neq 0 \\ = 0; & \text{iff } u = 0, \end{cases} \tag{2.7}$$

Positive-definiteness of a linear operator L ascertains a unique solution.

To minimize the functional (2.5), one can use different methods. For instance, the Rayleigh-Ritz method is a direct method which uses the linear property of the operator L. First, the unknown u is expressed as a linear combination of trial or basis functions:

$$U_n(r) = \sum_{i=1}^{n} a_i u_i(r)\,, \tag{2.8}$$

where each basis function u_i satisfies the boundary conditions and the coefficients a_i are the unknowns to be determined.

The Rayleigh-Ritz method approach concerns a specific class of operators, namely, *positive-definite bounded below*. Which implies that the operator L is positive-definite and if there exists a positive number γ^2 such that

$$\langle \mathrm{L}u, u\rangle \geq \gamma^2 \langle u, u\rangle\,, \tag{2.9}$$

for all u, then L is considered as *bounded below*. With this two constrains, it guarantees that for (2.2), the solution is unique and it is the minimizing solution for the functional (2.3) [23].

All trial functions used in (2.5) must satisfy the Dirichlet boundary conditions while Neumann boundary conditions are natural and do not have to be imposed. Inserting (2.8) into (2.3) yields a matric equation whose unknowns are the a_i's.

Using the matrix notation

$$\underline{a}^t = [a_1, a_2, \ldots, a_n], \tag{2.10}$$

we can write

$$U_n = \underline{a}^t \underline{u} = \underline{u}^t \underline{a}, \tag{2.11}$$

where $\underline{a}$ and $\underline{u}$ are column matrix having n elements each. Now insert the trial function into the functional, one obtain

$$F(U_n) = \underline{a}^t \langle \mathrm{L}\underline{u}, \underline{u}^t \rangle \underline{a} - 2\underline{a}^t \langle \underline{u}, f \rangle . \tag{2.12}$$

To minimize the functional, we have to select $\underline{a}$ such that

$$\frac{\partial F(U_n)}{\partial \underline{a}_i} = 0 . \tag{2.13}$$

From (2.12)

$$\begin{aligned} \frac{\partial F}{\partial \underline{a}} &= \frac{\partial \underline{a}^t}{\partial \underline{a}} \Big(\langle \mathrm{L}\underline{u}, \underline{u}^t \rangle \underline{a} \Big) + \frac{\partial}{\partial \underline{a}} \Big(\langle \mathrm{L}\underline{u}, \underline{u}^t \rangle \underline{a} \Big)^t \underline{a} - 2 \frac{\partial \underline{a}^t}{\partial \underline{a}} \langle \underline{u}, f \rangle \\ &= \langle \mathrm{L}\underline{u}, \underline{u}^t \rangle \underline{a} + \frac{\partial}{\partial \underline{a}} \Big(\underline{a}^t \langle \mathrm{L}\underline{u}, \underline{u}^t \rangle^t \Big) \underline{a} - 2 \langle \underline{u}, f \rangle \\ &= \langle \mathrm{L}\underline{u}, \underline{u}^t \rangle \underline{a} + \langle \mathrm{L}\underline{u}, \underline{u}^t \rangle^t \underline{a} - 2 \langle \underline{u}, f \rangle . \end{aligned} \tag{2.14}$$

Since L is self-adjoint and the transpose of a matrix product equals the product of the transposed matrices in reverse order (2.14) becomes

$$\frac{\partial F}{\partial \underline{a}} = 2 \langle \mathrm{L}\underline{u}, \underline{u}^t \rangle \underline{a} - 2 \langle \underline{u}, f \rangle . \tag{2.15}$$

Hence, the minimum value of F is obtained by the condition:

$$\langle \mathrm{L}\underline{u}, \underline{u}^t \rangle \underline{a} = \langle \underline{u}, f \rangle , \tag{2.16}$$

which, in matrix notation, is written as

$$A\underline{a} = \underline{b} . \tag{2.16}$$

Due to the property of positive/negative definiteness, there is a unique solution for $\underline{a}$ [30]. Also due to self-adjointness, A is symmetric. Consequently, only the upper (or lower) triangular portion plus the diagonal terms of the matrix need to be computed.

The FEM approach uses an assemblage of functions defined only over finite regions to approximate the unknown in a piecewise fashion. The region is usually divided into triangles for two-dimensional problems and tetrahedrons for three-dimensional problems. Since Laplace's equation must be solved, the functional is formed by the summation of all the sub-functionals corresponding to each triangle or subregion. Thus from (2.5):

$$F = \sum_t F_t = \sum_t \int_{\Omega_t} \epsilon_t (\nabla \phi)^2 \, d\Omega \,, \tag{2.18}$$

where the permittivity ϵ_t is assumed constant in each subregion but may vary from subregion to subregion, to accomplish the interface conditions for inhomogeneous problems.

2.3.1 Single element

It is best to consider a single element, (shown in Fig. 2.1) and then, move to the more general structure. For two-dimensional problems, the potential in each triangle is approximated by a polynomial in the two space coordinates x and y. For a linear approximation, the trial function becomes:

$$\phi(x, y) = c_0 + c_1 x + c_2 y \,, \tag{2.19}$$

where there is a total of three variational parameters per triangle.

It is preferable to express ϕ in terms of the node potentials ϕ_i, ϕ_j, and ϕ_k. With (2.19), this can be written in the matrix form :

$$\begin{pmatrix} 1 & x_i & y_i \\ 1 & x_j & y_j \\ 1 & x_k & y_k \end{pmatrix} \begin{pmatrix} c_0 \\ c_1 \\ c_2 \end{pmatrix} = \begin{pmatrix} \phi_i \\ \phi_j \\ \phi_k \end{pmatrix}, \tag{2.20}$$

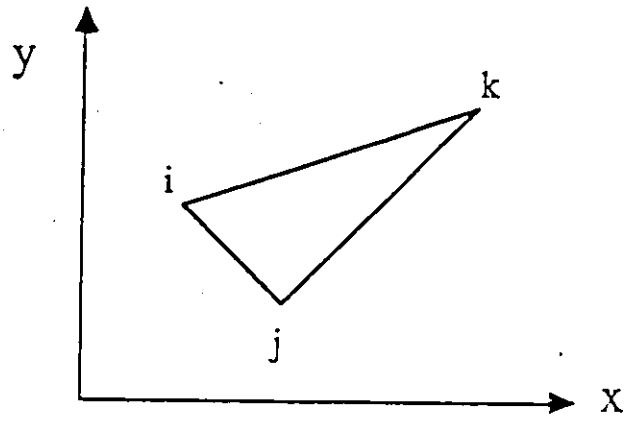

Fig.2.1 A single first-order element for the FEM procedure.

Using Cramer's rule, the unknown coefficients c_n $(n = 0, 1, 2)$ are given by

$$\begin{aligned}
c_0 &= \left\{ \phi_i \begin{vmatrix} x_j & y_j \\ x_k & y_k \end{vmatrix} + \phi_j \begin{vmatrix} x_k & y_k \\ x_i & y_i \end{vmatrix} + \phi_k \begin{vmatrix} x_i & y_i \\ x_j & y_j \end{vmatrix} \right\} /2A \\
c_1 &= \left\{ \phi_i \begin{vmatrix} 1 & y_k \\ 1 & y_j \end{vmatrix} + \phi_j \begin{vmatrix} 1 & y_i \\ 1 & y_k \end{vmatrix} + \phi_k \begin{vmatrix} 1 & y_j \\ 1 & y_i \end{vmatrix} \right\} /2A \\
c_2 &= \left\{ \phi_i \begin{vmatrix} 1 & x_j \\ 1 & x_k \end{vmatrix} + \phi_j \begin{vmatrix} 1 & x_k \\ 1 & x_i \end{vmatrix} + \phi_k \begin{vmatrix} 1 & x_i \\ 1 & x_j \end{vmatrix} \right\} /2A ,
\end{aligned} \tag{2.21}$$

where A is the area of the triangle.

Substituting this back into (2.19), we obtain

$$\begin{aligned}
\phi = \Big\{ & \left[(x_j y_k - x_k y_j) + (y_j - y_k)x + (x_k - x_j)y \right] \phi_i \\
& + \left[(x_k y_i - x_i y_k) + (y_k - y_i)x + (x_i - x_k)y \right] \phi_j \\
& + \left[(x_i y_j - x_j y_i) + (y_i - y_j)x + (x_j - x_i)y \right] \phi_k \Big\} /2A ,
\end{aligned} \tag{2.22}$$

or

$$\phi(x, y) = a_i(x, y)\phi_i + a_j(x, y)\phi_j + a_k(x, y)\phi_k , \tag{2.23}$$

where $a_n(x,y)$, $n = i,j,k$ are linear interpolatory functions of the independent coordinates and are defined for the first-order approximation as follows:

$$a_i = \left[(x_j y_k - x_k y_j) + (y_j - y_k)x + (x_k - x_j)y\right]/2A\,, \tag{2.24}$$

where the subscripts may be circularly permuted in the sequence i,j,k. Note that at the position of the node i,

$$a_i(x_n,y_n) = \begin{cases} 1; & n = i \\ 0; & n = j \text{ or } k, \end{cases} \tag{2.25}$$

and along the triangle side joining node i to node j:

$$a_k(x,y) = 0\,. \tag{2.26}$$

This ensures that the potential is continuous between adjacent triangles. The potential along the triangle side joining nodes i to j is

$$\phi = a_i(x,y)\phi_i + a_j(x,y)\phi_j\,. \tag{2.27}$$

Hence, the Dirichlet condition can be satisfied by the properties of the trial function.

In two-dimensional Laplace's problem with $\epsilon = 1$, the functional (2.5) can approximately evaluated as follows

$$F = \int_{\substack{\text{single} \\ \text{element}}} (\nabla\phi)^2\,dx\,dy = (\nabla\phi)^2 A\,, \tag{2.28}$$

where

$$\begin{aligned}
(\nabla\phi)^2 &= (\nabla a_i\phi_i + \nabla a_j\phi_j + \nabla a_k\phi_k)^2 \\
&= \Big\{\left[(y_j - y_k)\vec{i} + (x_k - x_j)\vec{j}\right]\phi_i + \left[(y_k - y_i)\vec{i} + (x_i - x_k)\vec{j}\right]\phi_j \\
&\quad + \left[(y_i - y_j)\vec{i} + (x_j - x_i)\vec{j}\right]\phi_k\Big\}^2/4A^2 \\
&= \Big\{\left[(y_j - y_k)^2 + (x_k - x_j)^2\right]\phi_i^2 + \left[(y_k - y_i)^2 + (x_i - x_k)^2\right]\phi_j^2 \\
&\quad + \left[(y_k - y_j)^2 + (x_j - x_i)^2\right]\phi_k^2 \\
&\quad + 2\left[(y_j - y_k)(y_k - y_i) + (x_k - x_j)(x_i - x_k)\right]\phi_i\phi_j \\
&\quad + 2\left[(y_j - y_k)(y_i - y_j) + (x_k - x_j)(x_j - x_i)\right]\phi_i\phi_k \\
&\quad + 2\left[(y_k - y_i)(y_i - y_j) + (x_i - x_k)(x_j - x_i)\right]\phi_j\phi_k\Big\}/4A^2\,,
\end{aligned} \tag{2.29}$$

and A is the area of the single element. To minimize the functional (2.28), one has to take the derivative with respect to the unknowns:

$$\begin{aligned}\frac{\partial F}{\partial \phi_i} = \frac{1}{2A}\Big\{ & \left[(y_j - y_k)^2 + (x_k - x_j)^2\right]\phi_i \\ & + \left[(y_j - y_k)(y_k - y_i) + (x_k - x_j)(x_i - x_k)\right]\phi_j \\ & + \left[(y_j - y_k)(y_i - y_j) + (x_k - x_j)(x_j - x_i)\right]\phi_k \,.\end{aligned} \tag{2.30}$$

The equations for $\frac{\partial F}{\partial \phi_j}$ and $\frac{\partial F}{\partial \phi_k}$ are derived in a similar manner. These equations can be written in matrix form as:

$$\frac{\partial F}{\partial \underline{\phi}} = \frac{1}{2} S \underline{\phi} = \frac{1}{2} \begin{pmatrix} s_{ii} & s_{ij} & s_{ik} \\ s_{ji} & s_{jj} & s_{jk} \\ s_{ki} & s_{kj} & s_{kk} \end{pmatrix} \begin{pmatrix} \phi_i \\ \phi_j \\ \phi_k \end{pmatrix} , \tag{2.31}$$

where the diagonal elements are given by

$$s_{ii} = \frac{1}{A}\left[(y_j - y_k)^2 + (x_j - x_k)^2\right] , \tag{2.32}$$

and the off-diagonal elements by

$$s_{ij} = -\frac{1}{A}\left[(y_i - y_k)(y_j - y_k) + (x_i - x_k)(x_j - x_k)\right] . \tag{2.33}$$

If one deals with dielectric subregions, the permittivity of the region defined by a triangle, in which it is supposed constant, will multiply (2.31).

Note that the matrix S is symmetric. This can be easily seen by interchanging i and j in (2.33). In order to find the stationary point of the functional (2.12), it was mentioned before that (2.31) must be set to zero, which yields

$$\begin{pmatrix} s_{ii} & s_{ij} & s_{ik} \\ s_{ji} & s_{jj} & s_{jk} \\ s_{ki} & s_{kj} & s_{kk} \end{pmatrix} \begin{pmatrix} \phi_i \\ \phi_j \\ \phi_k \end{pmatrix} = \begin{pmatrix} 0 \\ 0 \\ 0 \end{pmatrix} . \tag{2.34}$$

For the triangle subregions having a node point on a Dirichlet boundary, the potential at this node point is known, say g_i, and is not a variational parameter. Consequently, (2.34) can be written in the following matrix form:

$$\begin{pmatrix} s_{ji} & s_{jj} & s_{jk} \\ s_{ki} & s_{kj} & s_{kk} \end{pmatrix} \begin{pmatrix} g_i \\ \phi_j \\ \phi_k \end{pmatrix} = \begin{pmatrix} 0 \\ 0 \end{pmatrix} , \tag{2.35}$$

Finally, after rearrangement, one obtains the final systems to be solved:

$$\begin{pmatrix} s_{jj} & s_{jk} \\ s_{kj} & s_{kk} \end{pmatrix} \begin{pmatrix} \phi_j \\ \phi_k \end{pmatrix} = \begin{pmatrix} -g_i s_{ji} \\ -g_i s_{ki} \end{pmatrix}, \tag{2.36}$$

for each triangle, having one node on a Dirichlet boundary. Finally, for triangles having two nodes on a Dirichlet boundary where the potentials (say $\phi_i = g_i$ and $\phi_j = g_j$) are known, (2.34) becomes

$$(s_{kk})(\phi_k) = (-g_i s_{ki} - g_j s_{kj}). \tag{2.37}$$

A general matrix relation can now be written for the whole structure, accounting for all triangles:

$$[S][\phi] = [b], \tag{2.38}$$

in which $[S]$ is a $n \times n$ symmetric matrix, where n is the number of nodes at which the potential is unknown, $[\phi]$ is a column vector containing the unknown node potentials and $[b]$ is a column vector produced by the known Dirichlet boundary conditions. Then, the unknowns can be solved, using standard techniques such as the Gauss elimination method.

After solving (2.38), the potential and the electric field at any point in a triangle can be evaluated as follows:

i) From the potential of the three vertices, the unknown coefficients c_0, c_1, c_2 are obtained by solving (2.20).

ii) The potential at any point within the triangle is found from (2.19).

iii) The field is calculated by:

$$\frac{(\phi_2 - \phi_1)}{\Delta l} = E, \tag{2.39}$$

where the direction of the field is shown by Fig. 2.2.

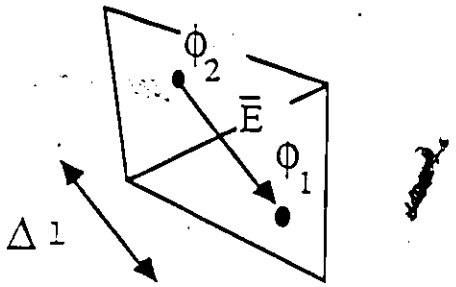

Fig. 2.2 Field direction between two elements.

2.4 Boundary Element Method

The BEM is a technique which offers an important potential advantage over other types of solutions, such as the FEM and the finite differences method. This is due to the fact that the BEM lowers the dimension of the problem by one unit, i.e., from *domain* types to *boundary* types of problem. This, generally, requires much smaller systems of equations to solve. Also, the amount of data to be manipulated is correspondingly reduced. This method is also well suited for unbounded domains, where other methods require approximated boundary conditions.

2.4.1 Integral Equation Formulations

For a source of unit strength located at the point r', the corresponding potential $G(r, r')$ satisfies the differential equation [29]

$$\nabla^2 G = -\delta(r - r') . \tag{2.40}$$

The Green's function G is a function of both the point of observation and the source point. If G is required to possess spherical symmetry and to vanish for $|r| = \infty$,

(2.40) is uniquely solved by the free space Green's function

$$G(r, r') = \frac{1}{4\pi|r - r'|}, \tag{2.41}$$

which is valid for an n-dimensional space, where $n \geq 3$, (except for the coefficient $1/4\pi$). For two dimensional problem ($n = 2$), the Green's function is

$$G(r, r') = -\frac{1}{2\pi} \log|r - r'|. \tag{2.42}$$

Once the solution for a unit source is known, the solution for any given arbitrary source distribution follows at once by superposition, i.e.,

$$\phi(r) = \frac{1}{\varepsilon} \int_v G(r, r')\rho(r')\, dv', \tag{2.43}$$

where ρ is the volume charge density.

Now, consider the case where the charges are distributed on a surface S with a surface density $\sigma(s)$. This type of distribution is called simple layer charge distribution. Thus the integral (2.43) has to be performed on a surface where the single layer distribution exist, which yields:

$$\phi(r) = \int_s G(r, s')\sigma(s')\, ds', \tag{2.44}$$

where the Green's function is given by (2.41), or by (2.42) for two-dimensional problem. This integral is well defined for all $r \notin s$ and satifies $\nabla^2\phi = 0$.

If the observation point is on the surface, one can show [29] that the above integral remains bounded (Dirichlet condition) . Thus (2.44) becomes

$$\int_s G(s, s')\sigma(s')\, ds' = \phi(s) = g(s), \tag{2.45}$$

where $g(s)$ is the known potential on the surface S. One can write (2.45), in the operator form or as an operator equation

$$\mathrm{K}\sigma = g. \tag{2.46}$$

The three-dimensional nature of (2.44) is transformed into a two-dimensional integral equation, which is called a Fredholm integral equation of the first kind. For a given Dirichlet boundary condition, $\sigma(s)$ can be solved using (2.45). Then ϕ is found everywhere using (2.44). The integral operator in (2.46) is self-adjoint (due to the symmetry of the kernel) and positive-definite, the corresponding functional of (2.46) is thus given by [24]:

$$F = \int_s \int_s \sigma(s)\sigma(s')G(s,s')\,ds'\,ds - 2\int_s \sigma(s)\phi(s)\,ds\,, \tag{2.47}$$

where the integration takes place over all charges. The function $\sigma(s)$ that minimizes (2.47) is also the solution of (2.46). For instance, it can be found by using the Rayleigh-Ritz method. Alternatively, (2.46) can be directly solved by using a moment method procedure. For a two-dimensional problem, integrations take place over linear distributions of charges, and the Green's function is given by (2.44).

When dielectrics are introduced, their effects are replaced by an equivalent fictitious single layer distribution of charges. The normal derivative of the potential at any point outside S is given by

$$\frac{\partial \phi}{\partial n}(r) = \int_s \sigma(r)\frac{\partial G}{\partial n'}(r,s')\,ds'\,. \tag{2.48}$$

If r is on S, Stakgold [29] showed that the normal derivative is discontinuous and the potential (Neumann condition) is given by

$$\frac{\partial \phi}{\partial n}(s) = \pm\frac{1}{2}\sigma(s) + \int_s \sigma(s')\frac{\partial G}{\partial n'}(s,s')\,ds'\,, \qquad s \in S\,, \tag{2.49}$$

where the sign depends on the direction of the normal of S. Equation (2.49) is a Fredholm integral equation of the second kind. If Neumann boundary conditions are known on S, (2.49) can be solved for the fictitious charge density $\sigma(s)$ (referred sometime as polarization charge density). However, one shall see that it is not necessary to introduce the Neumann boundary conditions.

On either side of the interface, (2.49) is written as

$$\frac{\partial \phi}{\partial n_1}(s) = \frac{\sigma(s)}{2} + \int_s \sigma(s') \frac{\partial G}{\partial n'}(s, s')\, ds' , \tag{2.50a}$$

and

$$\frac{\partial \phi}{\partial n_2}(s) = -\frac{\sigma(s)}{2} + \int_s \sigma(s') \frac{\partial G}{\partial n'}(s, s')\, ds' , \tag{2.50b}$$

where the normals n_1 and n_2 point towards and away from the interface respectively, as shown in Fig. 2.3

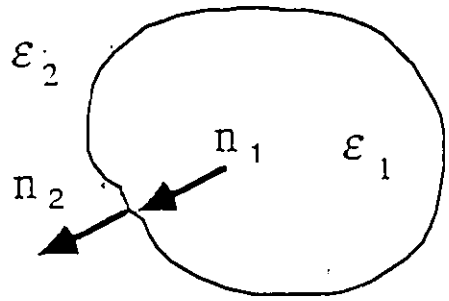

Fig.2.3 Geometry of Integral Equation-problem.

Substituting (2.50b) from (2.50a) yields the polarization charge distribution

$$\sigma(s) = \frac{\partial \phi}{\partial n_1}(s) - \frac{\partial \phi}{\partial n_2}(s) . \tag{2.51}$$

This expression illustrates that the discontinuity of the electric field normal component across a dielectric interface, can be described by a fictitious surface charge distribution. Finally, one has to introduce the interface condition

$$\varepsilon_1 \frac{\partial \phi}{\partial n_1}(s) = \varepsilon_2 \frac{\partial \phi}{\partial n_2}(s) , \tag{2.52}$$

where ε_1 and ε_2 are the permittivities on either side of the interface. This assumes the continuity of the normal component of the displacement field across the interface. Indeed, one shall remember that only fictitious or polarization charges exist on dielectric interfaces. Substituting (2.50) into (2.52) yields the operator equation

$$\mathrm{K}\sigma(s) = \frac{\varepsilon_2 + \varepsilon_1}{2}\sigma(s) + (\varepsilon_2 - \varepsilon_1)\int_s \sigma(s')\frac{\partial G}{\partial n}(s,s')\,ds' = 0\,. \tag{2.53}$$

Thus, if one specifies the potential values at the conductor surfaces S_C and calls S_I the interface between media of different permittivities, from (2.48) and (2.53) one has to solve the following coupled integral equations:

$$\int_{S_C+S_I} \sigma(s')G(s,s')\,ds' = \phi(s)\,, \qquad s \text{ on } S_C\,, \tag{2.54}$$

$$\frac{\varepsilon_1 + \varepsilon_2}{2}\sigma(s) + (\varepsilon_1 - \varepsilon_2)\int_{S_C+S_I} \sigma(s')\frac{\partial G}{\partial n}(s,s')\,ds' = 0\,, \qquad s \text{ on } S_I\,. \tag{2.55}$$

These two equations can be solved, for instance, using the Method of Moments, which includes the Galerkin and the point matching (collocation) methods [29]. Unfortunately, the operator in (2.55) is not self-adjoint because of the non-symmetric kernel. Consequently, Rayleigh-Ritz procedure may not converge, since the stationarity of the functional is not verified in this case.

The major disadvantage of BEM, as compare to FEM, is that the potential is not calculated directly from the known boundary condition. Instead, the charge distribution, σ, has to be evaluated first, and then the potential is found by (2.44) where the integration takes place on all charge distributions, real and fictitious.

2.5 Application to Finline Structures

A general illustration of finline structures with their waveguide enclosure is shown in Fig. 2.4. Slot is etched on the conductor on a dielectric substrate (usually RT-Duroid) which is used for mechanical support. The planar structure is sandwiched between two halves of a waveguide, in the E-plane of the dominant mode.

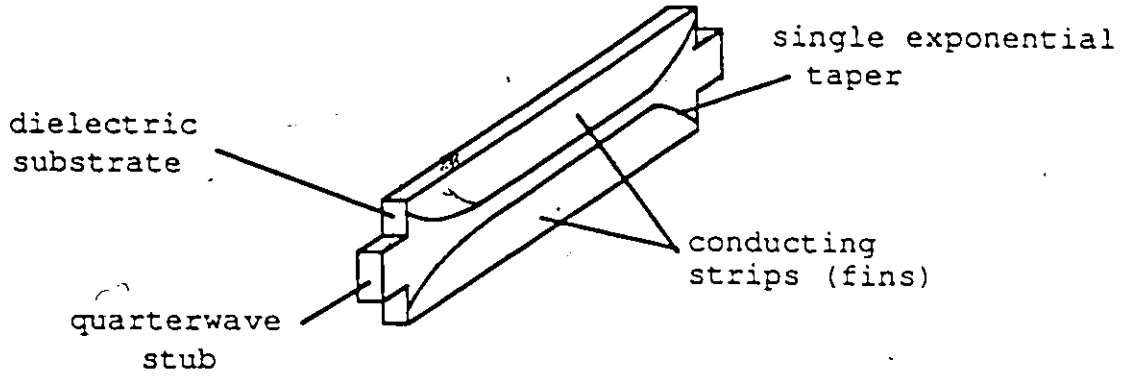

a) Finline insert with two exponential transitions to waveguide

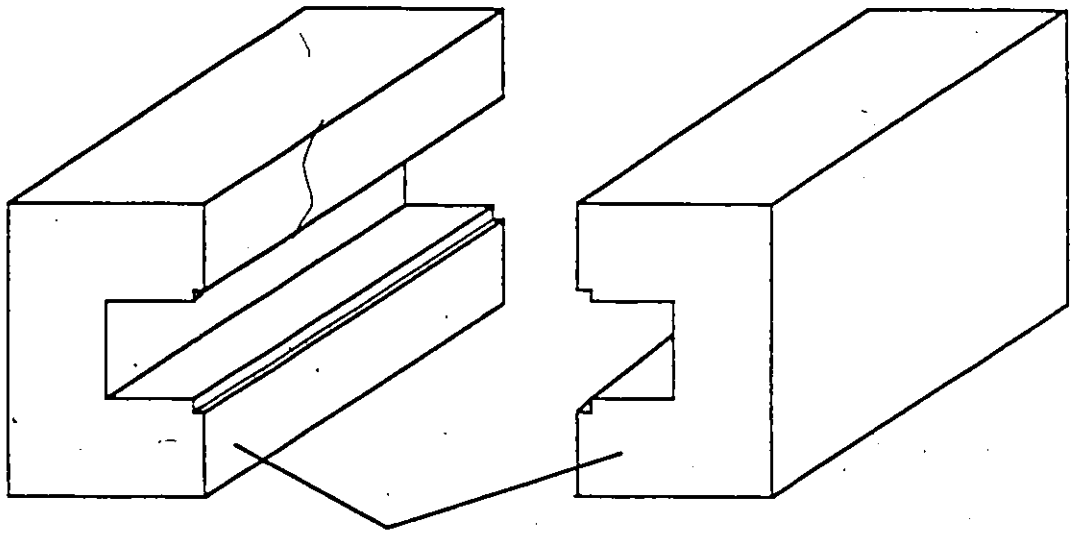

b) Finline housing with inner standard waveguide dimensions

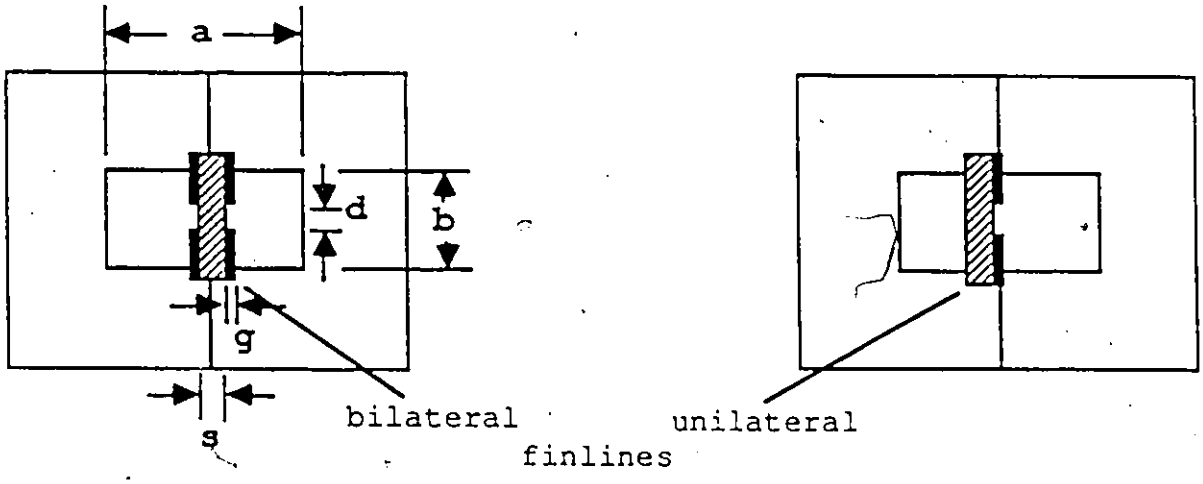

c) Cross-section of bilateral and unilateral finlines

Fig.2.4 Geometry of a typical E-plane line (Finline)

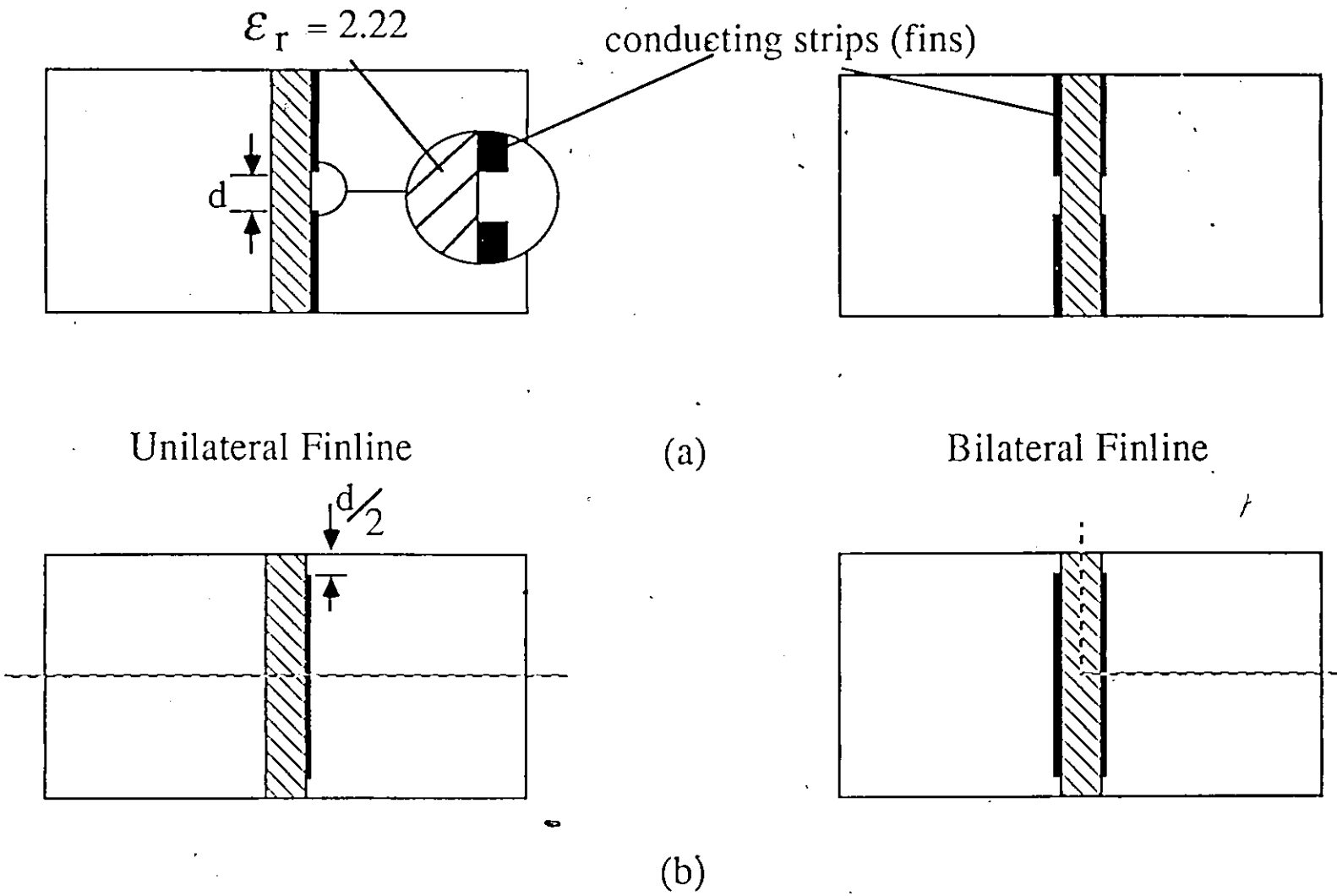

Fig.2.5 Unilateral and Bilateral Finline Structures (a) Reciprocal Structures (b).

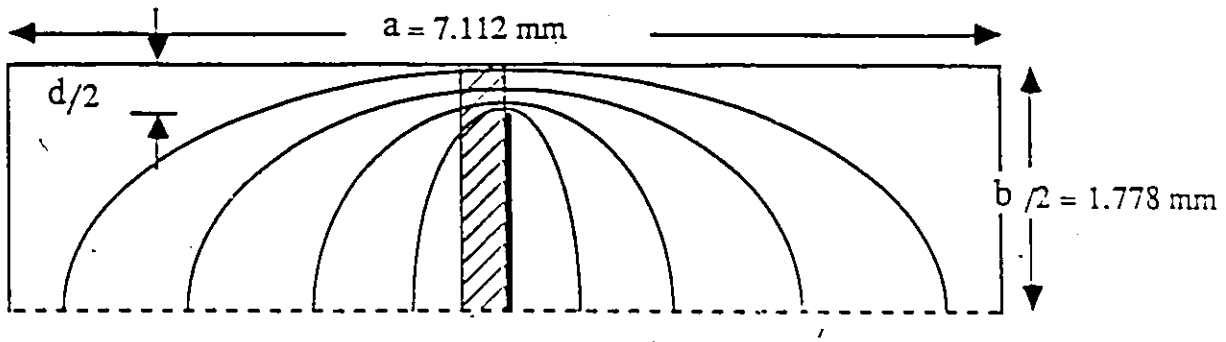

a) unilateral finline

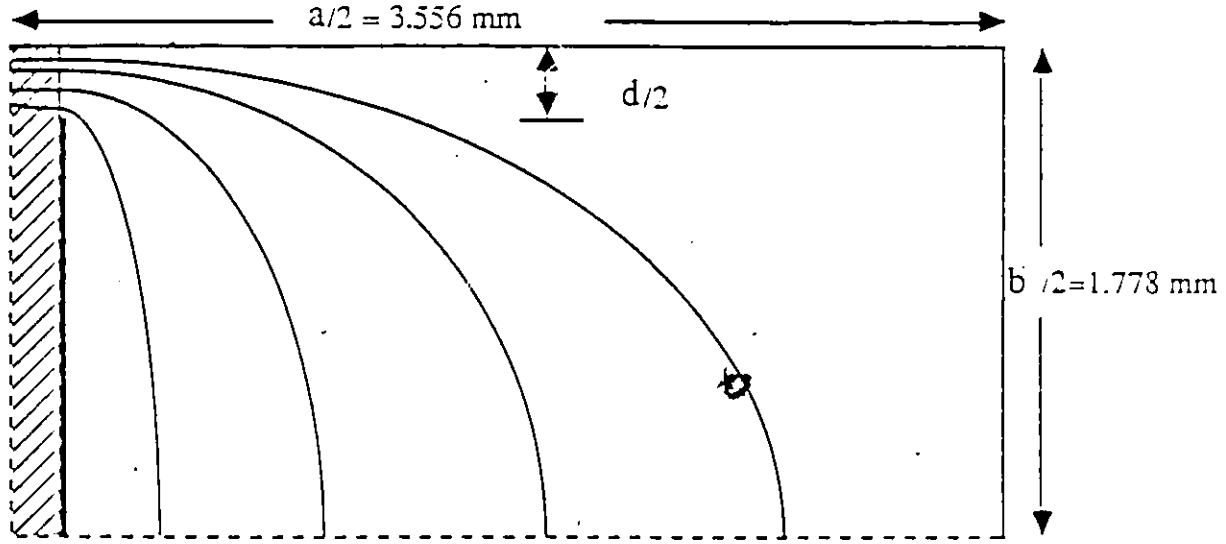

b) bilateral finline

Fig.2.6 Contour plot of equipotential lines for (a) unilateral and (b) bilateral finline reciprocal structures for WR-28, obtained with the BEM program. Gapwidth d =0.5 mm, conductor thickness g =17 μm and substrate thickness s =254 μm.

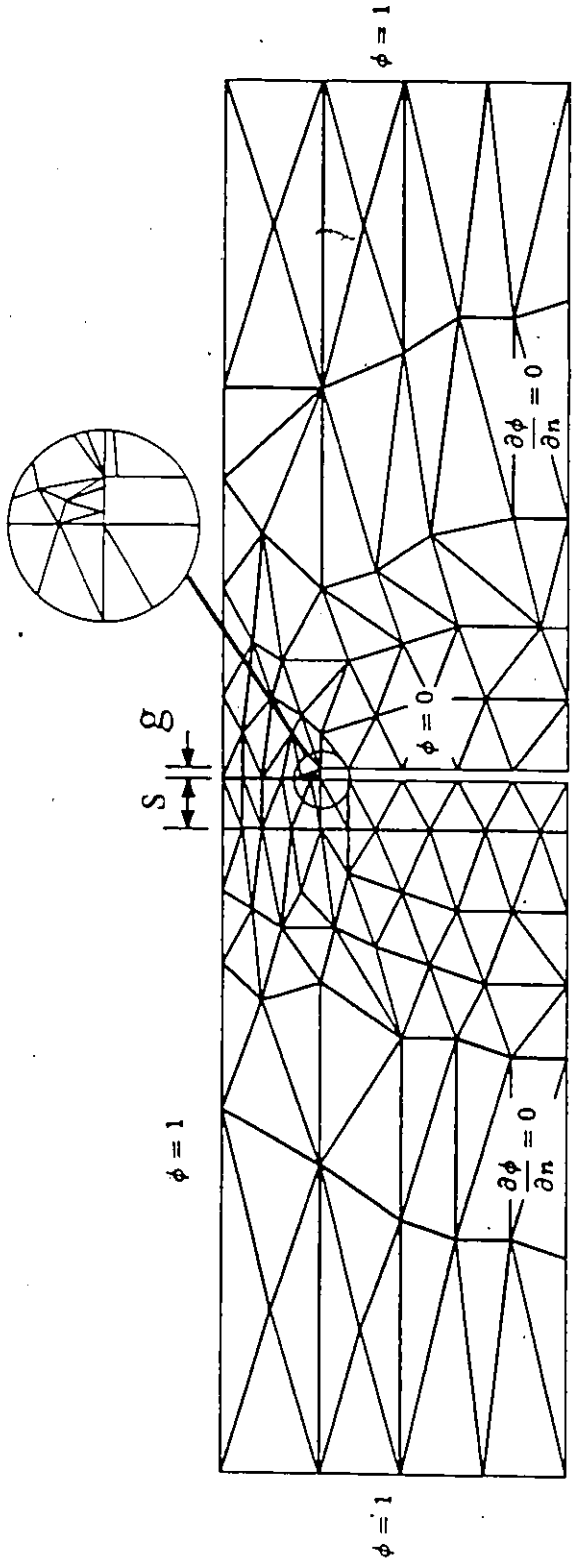

Fig.2.7 Half Reciprocal Structure of a Unilateral Finline divided into 163 triangles and 103 node points. Geometrical parameters same as in Fig.2.6a) except gapwidth d=1 mm.

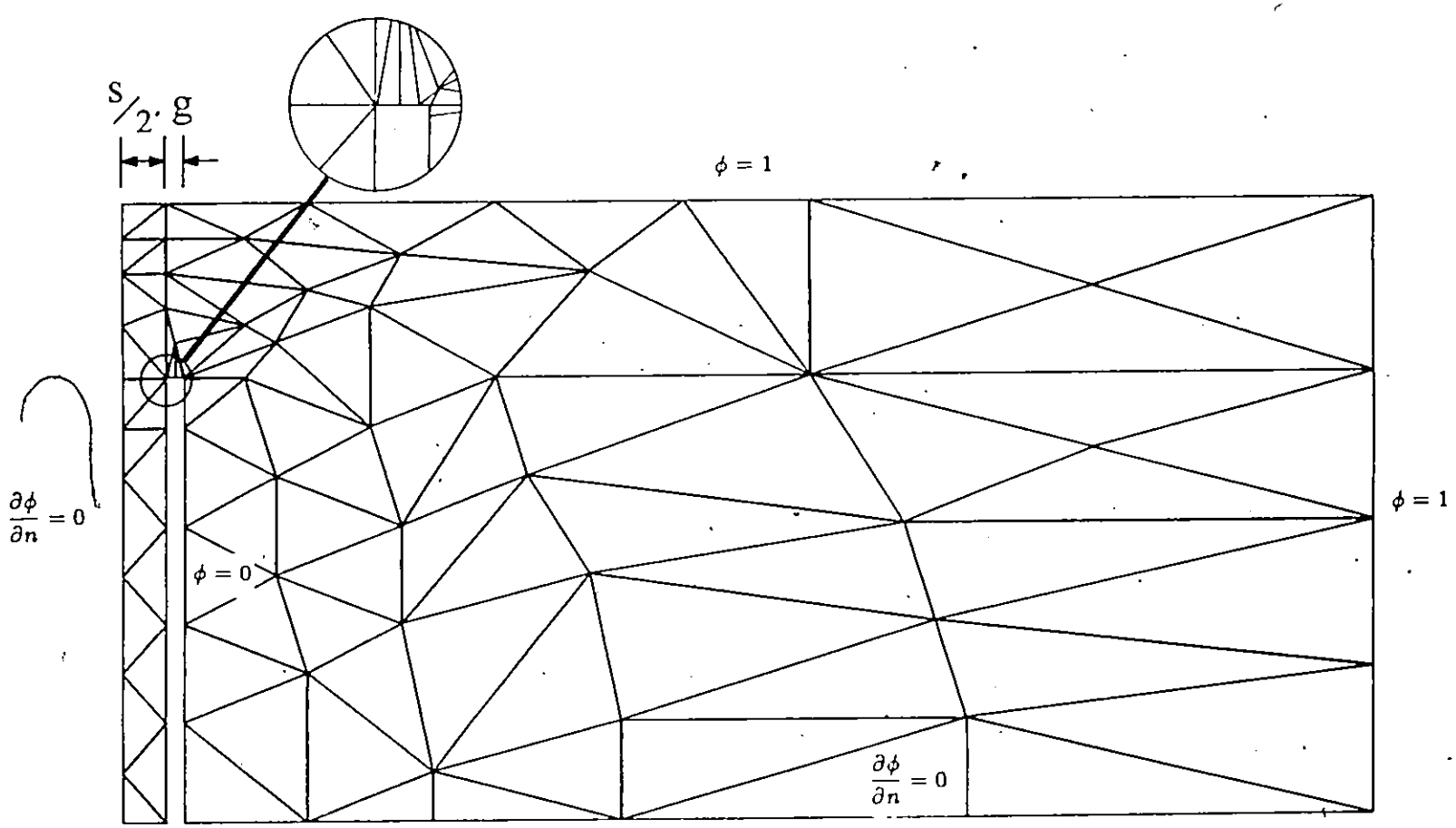

Fig.2.8 Quarter Reciprocal Structure of a Bilateral Finline divided into 100 triangles and 72 node points. Geometrical parameters same as in Fig.2.6b) except gapwidth d=1 mm.

The quantity of interest is the field in between the two conducting strips. If the gapwidth d is small as compared with the height b of the waveguide, one can use the image technique to obtain the structure shown in Fig. 2.5b), which is the reciprocal of the real structure shown in Fig. 2.5a). The potential between the two conducting strips at (a) is equal to twice the potential between the conducting strip and the waveguide housing for similar field value. Due to axial symmetry, only the part above the dotted line is considered. Dirichlet boundary conditions are given by the potential on the waveguide housing held arbitrarily at 1 volt, and the conducting strips held at O volt. The interface condition

$$\varepsilon_1 \frac{\partial \phi}{\partial n}\Big|_1 = \varepsilon_2 \frac{\partial \phi}{\partial n}\Big|_2, \tag{2.56}$$

is enforced at the interface between the dielectric substrate ($\varepsilon_1 = 2.22$ for RT-duroid) and the air ($\varepsilon_2 = 1$). For the open ended sides, the Neumann boundary condition is enforced.

$$\frac{\partial \phi}{\partial n}\Big|_s = h(s). \tag{2.57}$$

In particular, $h(s) = 0$ because the potential lines are perpendicular to the boundaries implying that the normal component of the electric field vanishes. This is illustrated by Fig. 2.6a) and 2.6b), which show the contour plot of equipotential lines, computed by the BEM, for the reciprocal structure of unilateral and bilateral finline, respectively. As expected, the field is concentrated in between the conductors (gap). The maximum field value is located at the sharp corner of the conductors.

In order to evaluate the field value for bilateral finlines with the FEM program, 100 triangles and 72 node points were used (see Fig. 2.7), while for unilateral finlines, 163 triangles and 103 node points were used (see Fig. 2.8). In order to obtain more accurate results, the triangle node points must be located as close to the equipotential line as possible. This implies some *a priori* knowledge of the field distribution.

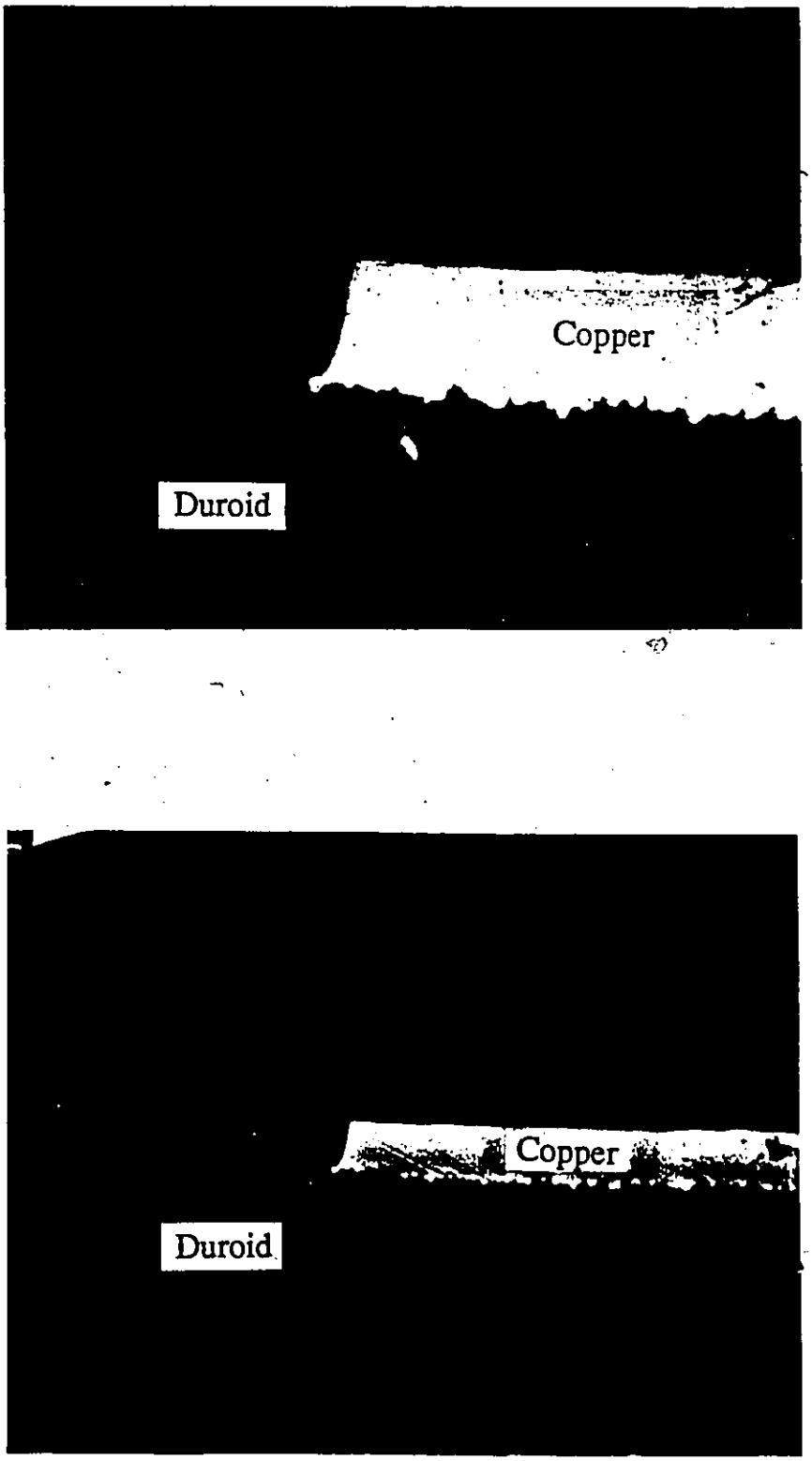

Fig.2.9 Optical Micrographs of a sectioned Finline structure.

2.6 Edge Profile

Realistic edge profiles were used, according to the observations made with an optical electronmicroscope (see Fig. 2.9). The profile shows sharp edges where the highest value of the electric field strength is expected. For simplicity, a right-angle edge profile was used to evaluate the field at the corner. However, singularity arose at the corner when the BEM was used. A modified edge profile had to be used, with radius of curvature approximately equal to 1 μm (see Fig. 2.10a).

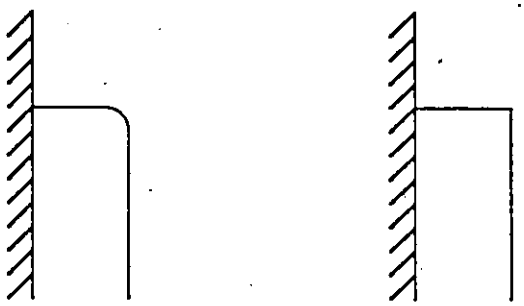

Fig.2.10 Edge profile used (a) in BEM and (b) in FEM.

However, for the FEM evaluations, realistic profiles could be approximated using right angle corners, as shown in Fig. 2.10b.

Chapter 3

RESULT

3.1 Introduction

This chapter presents the theoretical values obtained by using the Finite Element and the Boundary Element Methods. A 11/750 VAX computer was used for computations. The program listing for the FEM is given in the appendix. The listing of the program Greenfield2 [27], which uses the BEM, is not available since it is a commercial package. However, a brief description of the two programs will be given.

3.2 Simulation results with the FEM

3.2.1 Program Description

The FORTRAN program consists of two major parts, the first one constructs the system of equations and the second solves the system by using a Gauss elimination procedure. All operations were performed in double precision arithmetic to achieve the best possible accuracy.

3.2.2 Results

The maximum field values computed with the FEM, which are shown in Table 3.1, were determined for a voltage of one volt across the gap. The dimensions of the structures are shown in Table 3.3. As expected, they were located at the edges of the conductors.

For unilateral finlines, the maximum field values are very close for the two different waveguide housings. This verifies the assumption that the housing has little effect on the field configuration in between the fins, as long as the gapwidth is small.

d(mm)	housing	Bilateral (kV/m)	Unilateral (kV/m)
0.5	WR-90	16.3	8.39
1.0	WR-90	5.54	4.66
1.5	WR-90	3.17	3.40
2.0	WR-90	2.14	2.79
2.5	WR-90	1.59	2.42
0.5	WR-28	11.6	7.58
1.0	WR-28	5.03	5.03
1.5	WR-28	3.18	4.33
2.0	WR-28	2.36	4.06
2.5	WR-28	1.91	4.01

Table 3.1 Maximum field values of unilateral and bilateral finlines, evaluated by FEM for different gapwidths. WR-28 and WR-90 waveguide housings are considered with geometrical parameters given in Table 3.3.

However, for bilateral finlines, the field values obtained for WR-90 are larger than those obtained for the WR-28 housing. This may be due to the size of elements or subsections. Indeed, for both bilateral finlines, the number of triangles used to simulate the geometry of the structure were the same. Consequently, scaling the size of the triangles from one structure to another may also contribute to some errors in evaluating the potential around the conductor edges.

3.3 Simulation results with the BEM

3.3.1 Program description

The available BEM program is a computer software package capable of evaluating

the field value at anypoint of a given structure. Two-dimensional problems can be easily entered interactively. A maximum of 139 nodes points (although the manual mentions 300 node points capacity) can be placed on the boundary. The output can be displayed either on a graphic terminal (TEKTRONIX 4107), or on an ink-jet printer (TEKTRONIX 4695).

d(mm)	housing	Bilateral (kV/m)	Unilateral (kV/m)
0.5	WR-90	22.4	23.0
1.0	WR-90	14.8	15.7
1.5	WR-90	11.3	12.6
2.0	WR-90	9.44	10.6
2.5	WR-90	8.23	9.36
0.5	WR-28	21.3	23.5
1.0	WR-28	13.6	15.9
1.5	WR-28	10.7	12.8
2.0	WR-28	9.21	11.3
2.5	WR-28	8.35	10.7

Table 3.2 Maximum field values in unilateral and bilateral finlines, evaluated by BEM for different gapwidths. WR-28 and WR-90 waveguide housings are considered with geometrical parameters given in Table 3.3.

The maximum field values are shown in Table 3.2 for different gapwidths. One can observe that the field values have no significant change, from X to Ka-band. The reason is the same as mentioned earlier, i.e. for small gaps, the field is more concentrated in the central region and hence the housing does not have much effect on the results. One can also notice that as the gapwidth d decreases, the field value increases, this is obvious since the potential is held constant across the gap.

3.4 Comparison between the FEM and the BEM

Although the BEM is easier to use and generally yields smaller systems to be solved, as compared to other techniques, the results obtained near the edge are not accurate. This will be demonstrated by the low-frequency experiments. The approach of the BEM is to sample the boundary of each subregion. It is more appropriate to apply when one deals with homogeneous subregions (e.g. finlines). However, the Greenfield2 software program, which uses the BEM approach, has been found not suitable to solve structures with very thin subregions. On the other hand, the FEM yields much better results. It has the disadvantage of producing higher order systems, as compared to the BEM, for a given geometry with homogeneous subregions. However, for highly inhomogeneous subregions, FEM is definitively the most appropriate method. In addition, there is some freedom to sample the subregions with any polygonal shape by choosing various sizes of trianglar elements. This allows higher accuracy near the edge. Finally, the computation of different gapwidths between the conducting strips and sizes of waveguide is just a matter of scaling. This feature is more computer efficient.

As shown in Table 3.1–3.2, there are large discrepancies between the two methods, the BEM gives larger field values than the FEM in general. In the unilateral finline case, the difference is more obvious. Here, one can predict that the BEM will give a lower breakdown value as compare with the FEM. From Table 3.1 and 3.2, for both unilateral and bilateral finlines, narrower gapwidth produces larger field values. This is easily explained by the fact that since the potential across the gap is unchanged, the field strength between the gap increases as the gapwidth decreases.

Assuming a static breakdown field value of 3×10^6 V/m in the air, one can calculate the voltage at which air breakdown will occur. The corresponding power is then evaluated with (2.1). The characteristic impedance Z_0 is computed by using the SDM. Finline structures in WR-90(X-band) and WR-28(Ka-band) waveguide

	a(mm)	b(mm)	s(μm)	g(μm)
WR-28	7.112	3.556	254	17
WR-90	22.86	10.16	762	34

Table 3.3 Dimension used for WR-28 and WR-90 housing finline structures.

housings were analysed (see Table 3.3 for the dimensions).

The values of the characteristic impedance in both X and Ka-bands are shown in Fig. 3.1–3.4. Only the lower and upper range is given which corresponds to the lower and upper frequencies of the particular frequency band (X or Ka). For identical gapwidth, bilateral finlines have a lower impedance than unilateral finlines. Also, the impedance values for WR-28 housing are about twice as large as those of the WR-90 with the same gapwidth. In order to match other types of solid-state devices, impedance value larger than 300 ohms are seldom used.

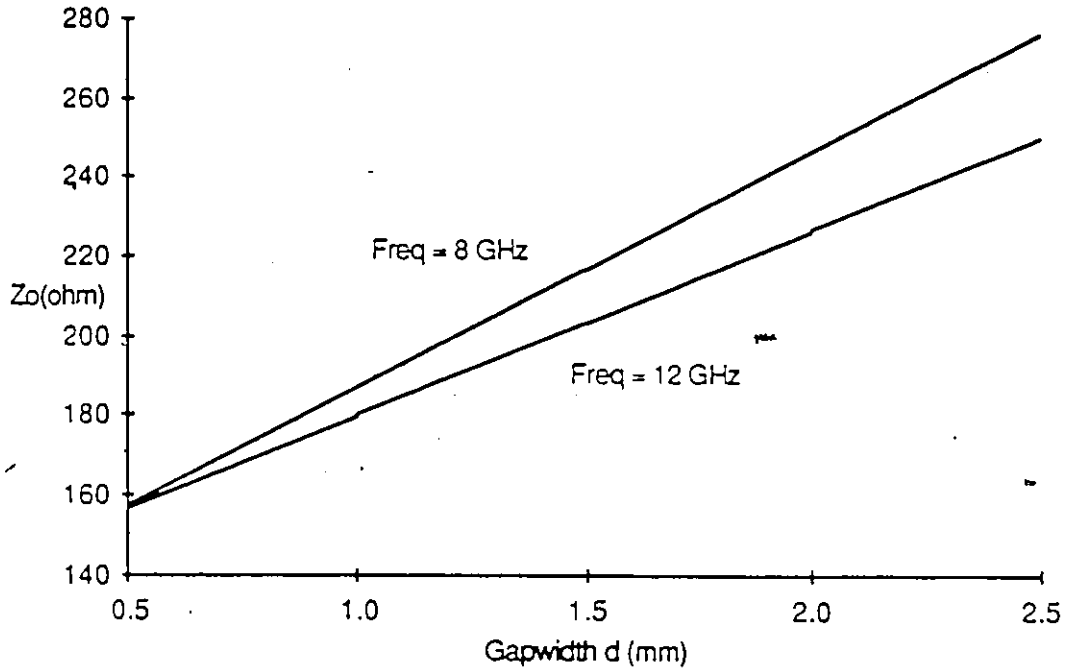

Fig.3.1 Impedance vs gapwidth for WR-90 unilateral finline structure evaluated by the SDM, s =762 μm, ε_r=2.22.

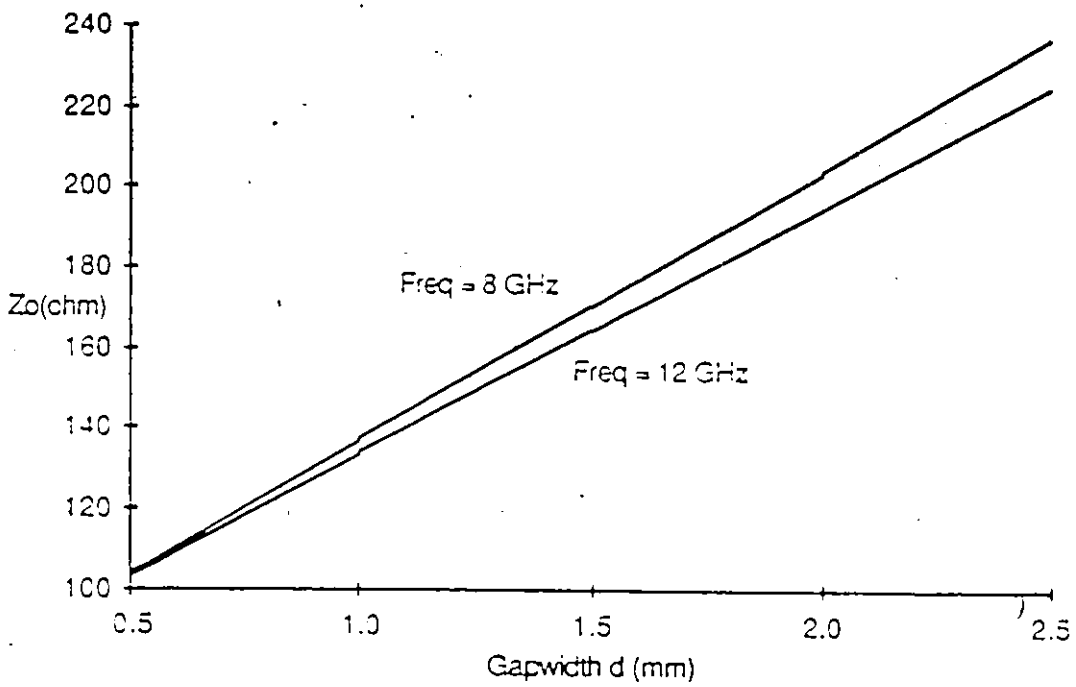

Fig.3.2 Impedance vs gapwidth for WR-90 bilateral finline structure evaluated by the SDM, s =762 μm, ε_r=2.22.

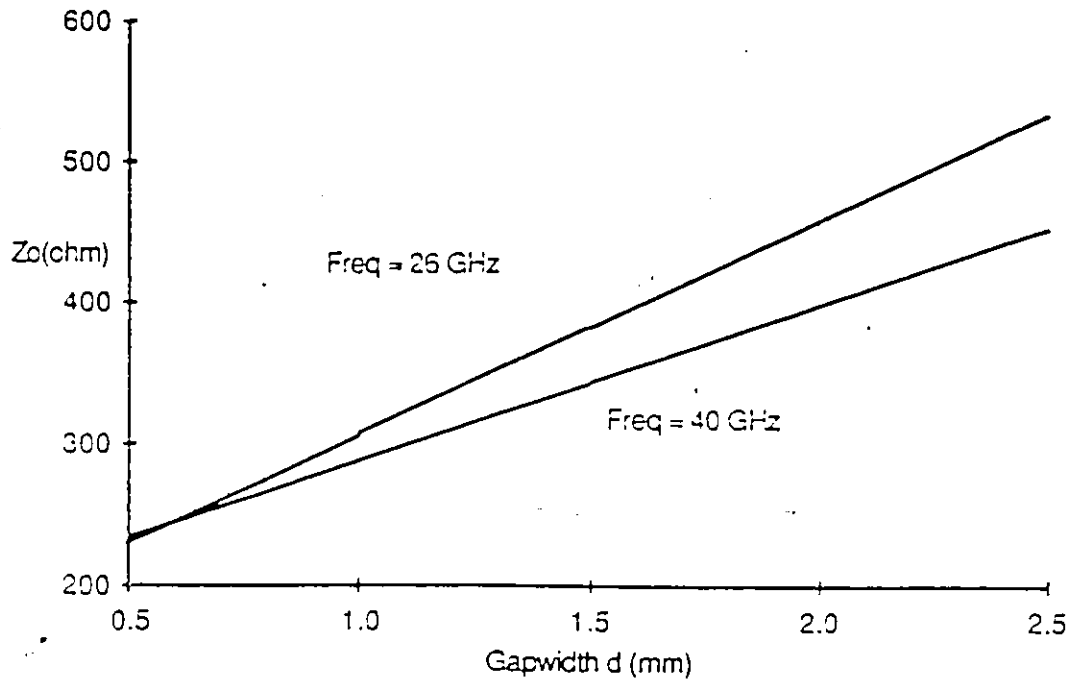

Fig.3.3 Impedance vs gapwidth for WR-28 unilateral finline structure evaluated by the SDM, s =254 μm, ε_r=2.22.

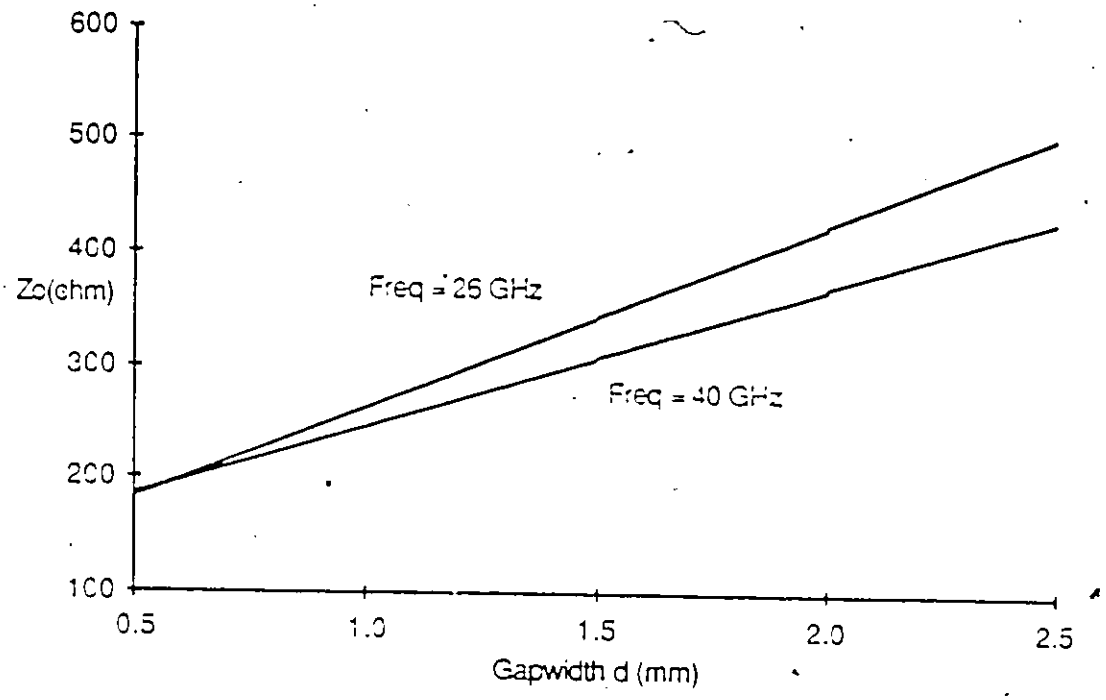

Fig.3.4 Impedance vs gapwidth for WR-28 bilateral finline structure evaluated by the SDM. s =254 μm, ε_r =2.22.

The simulated values for peak power-handling capacity of bilateral and unilateral finline structures are shown in Fig. 3.5–3.8, for both X and Ka-bands.

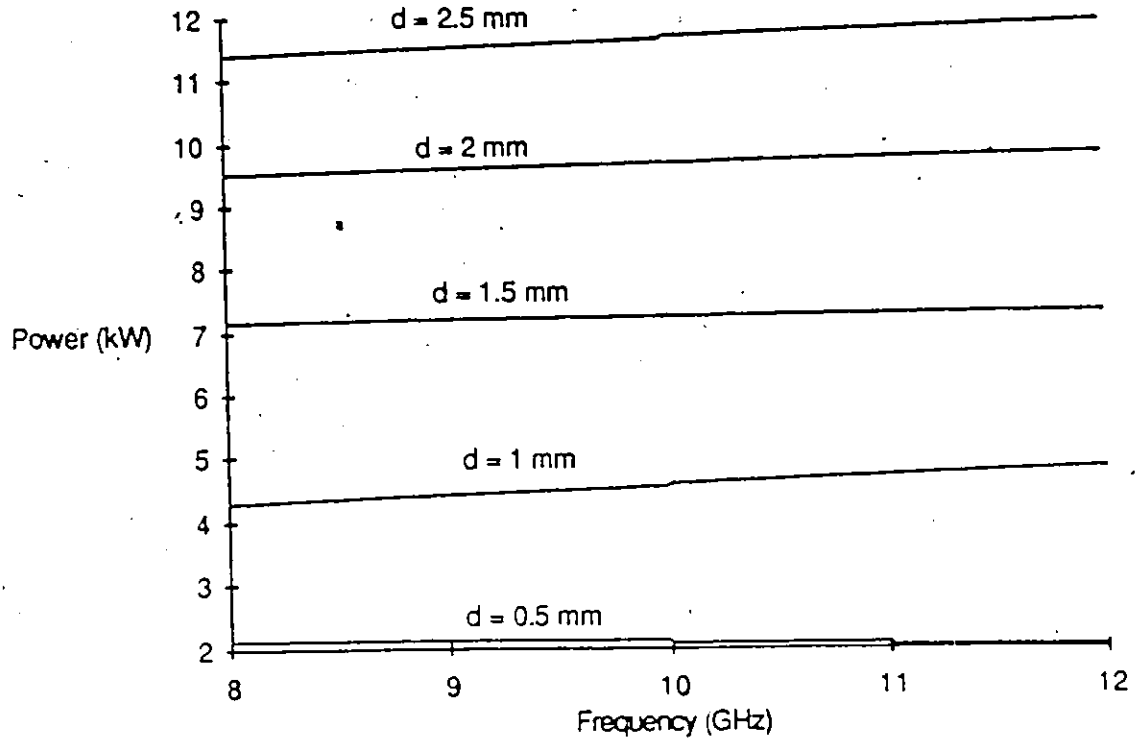

(a)

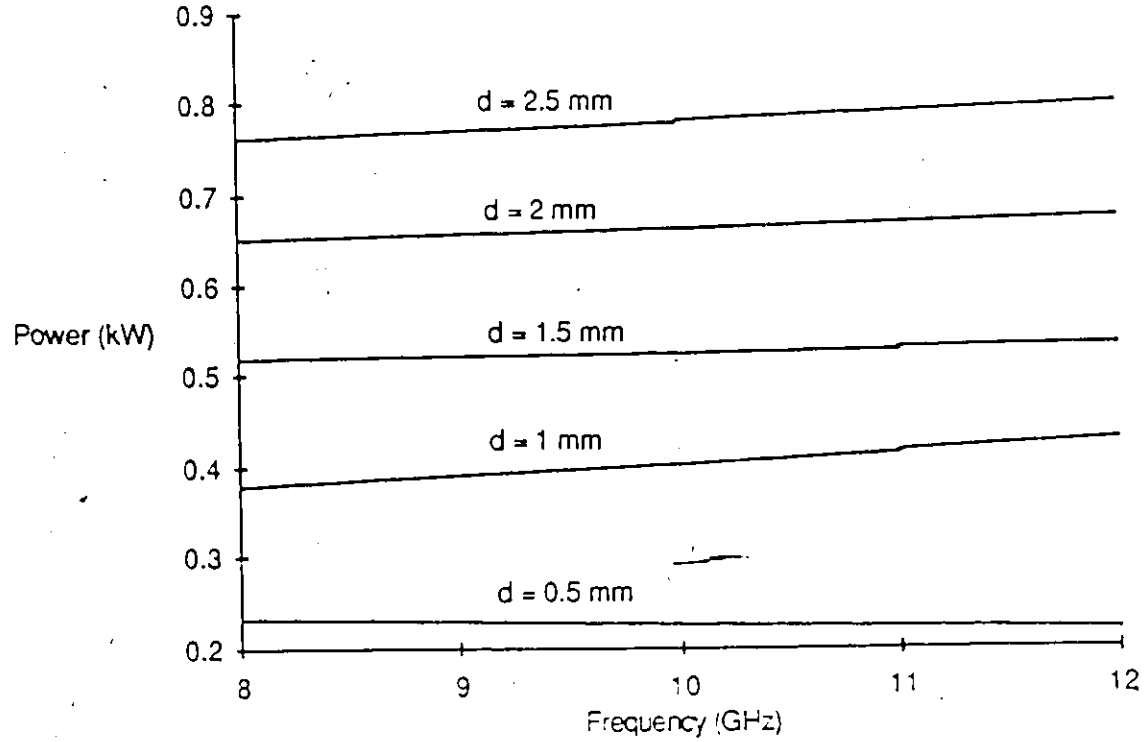

(b)

Fig.3.5 Peak power-handling capacity of WR-90 unilateral finline for different gapwidth, evaluated with (a) the FEM (b) the BEM, g=34 μm, s=762 μm, ε_r=2.22.

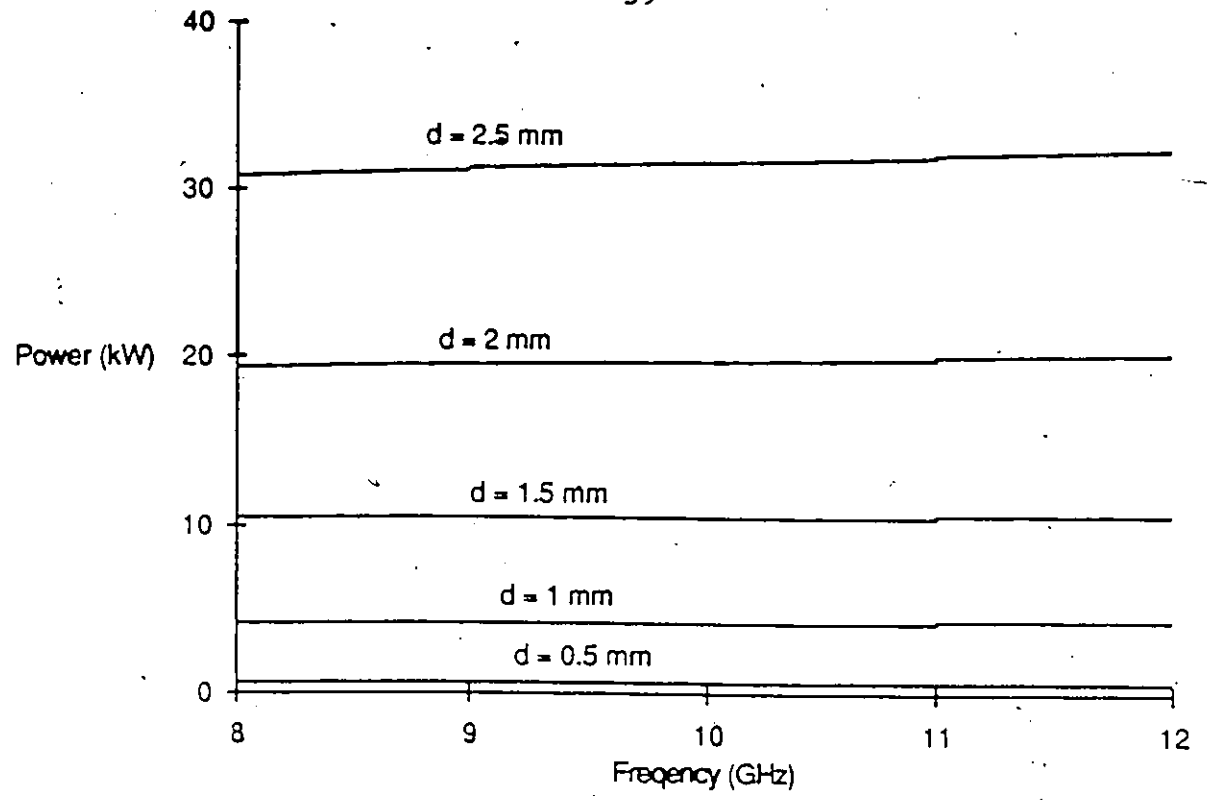

(a)

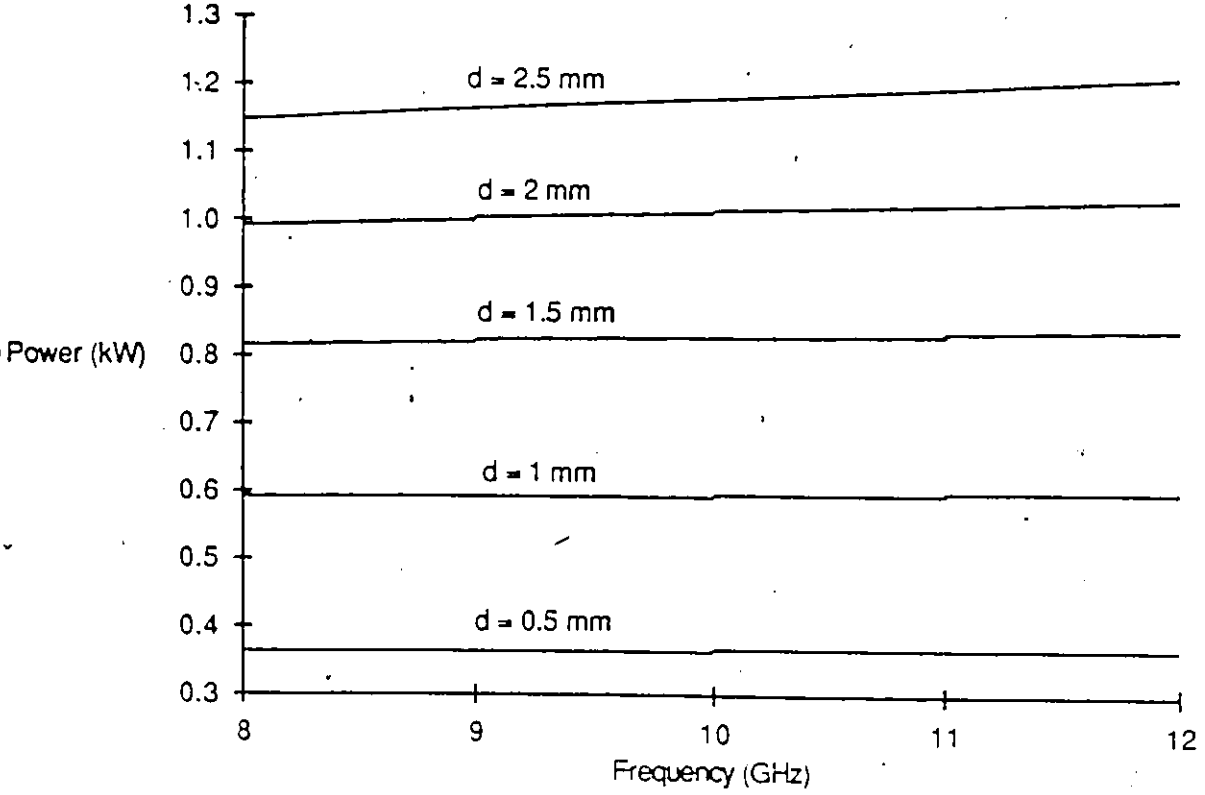

(b)

Fig.3.6 Peak power-handling capacity of WR-90 bilateral finline for different gapwidth, evaluated with (a) the FEM (b) the BEM, g=34 μm, s=762 μm, ε_r=2.22.

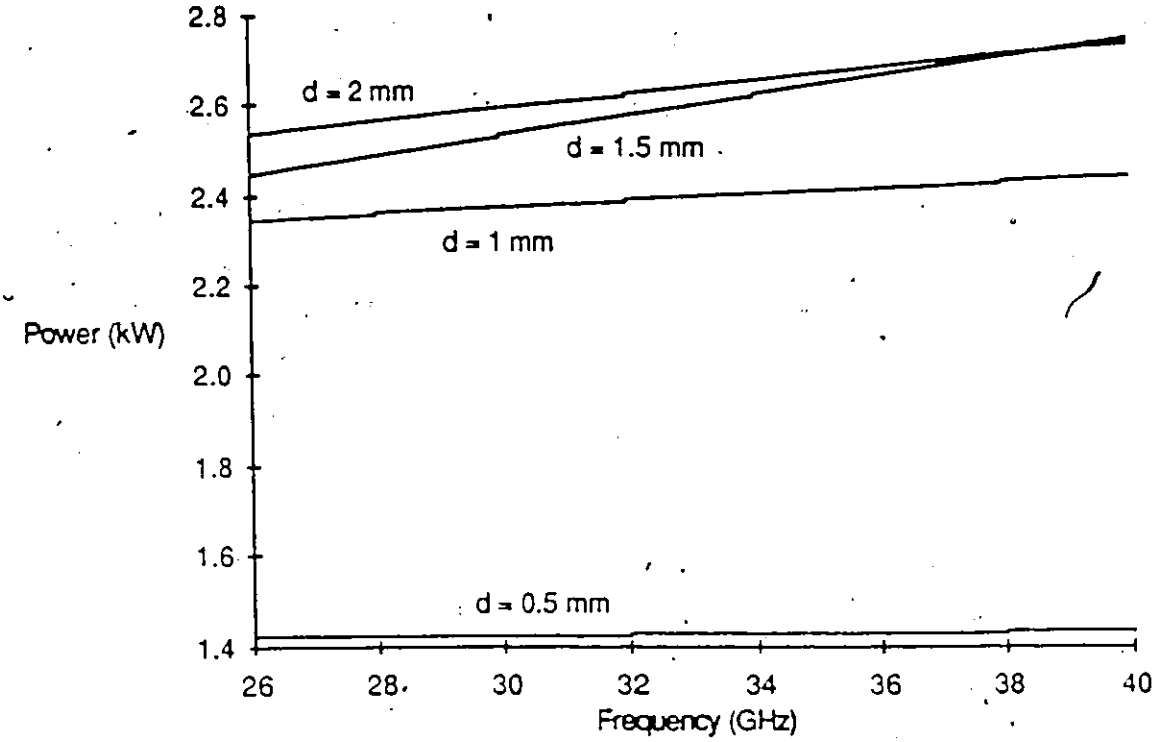

(a)

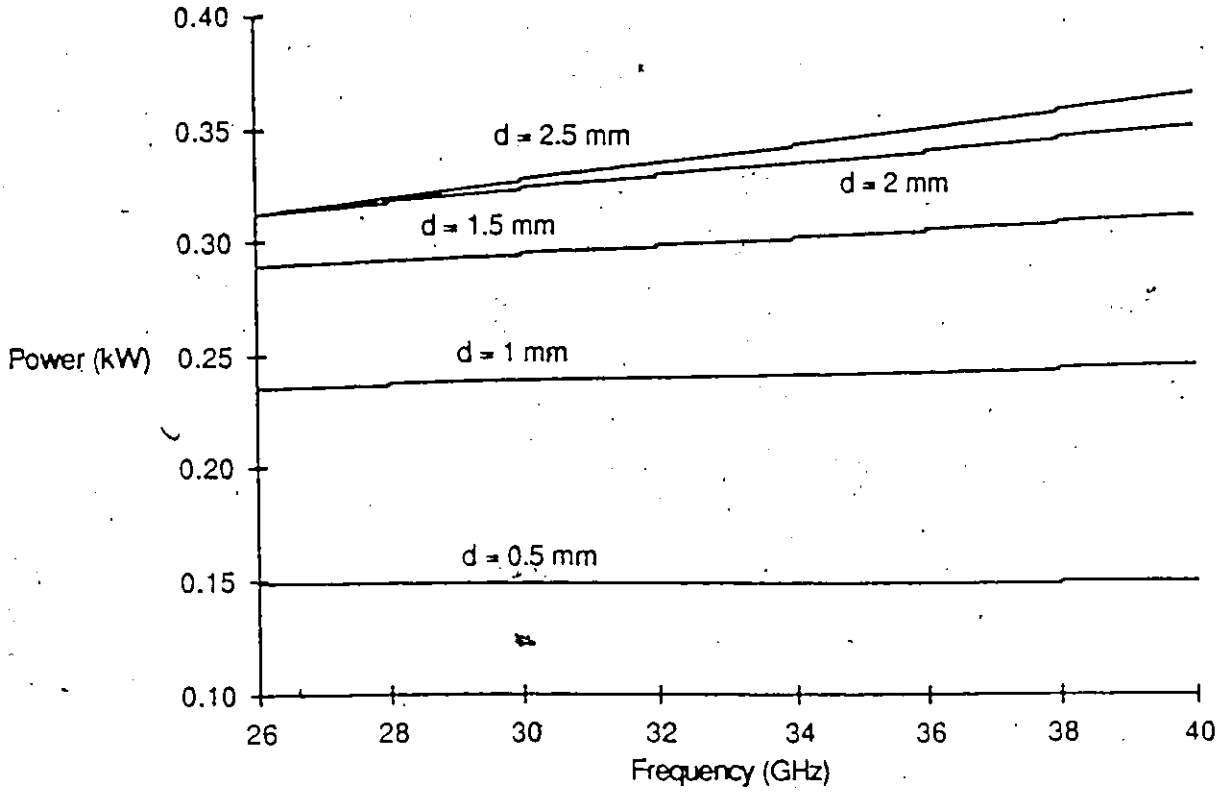

(b)

Fig.3.7 Peak power-handling capacity of WR-28 unilateral finline for different gapwidth, evaluated with (a) the FEM (b) the BEM, g=17 μm, s=254 μm, ε_r=2.22.

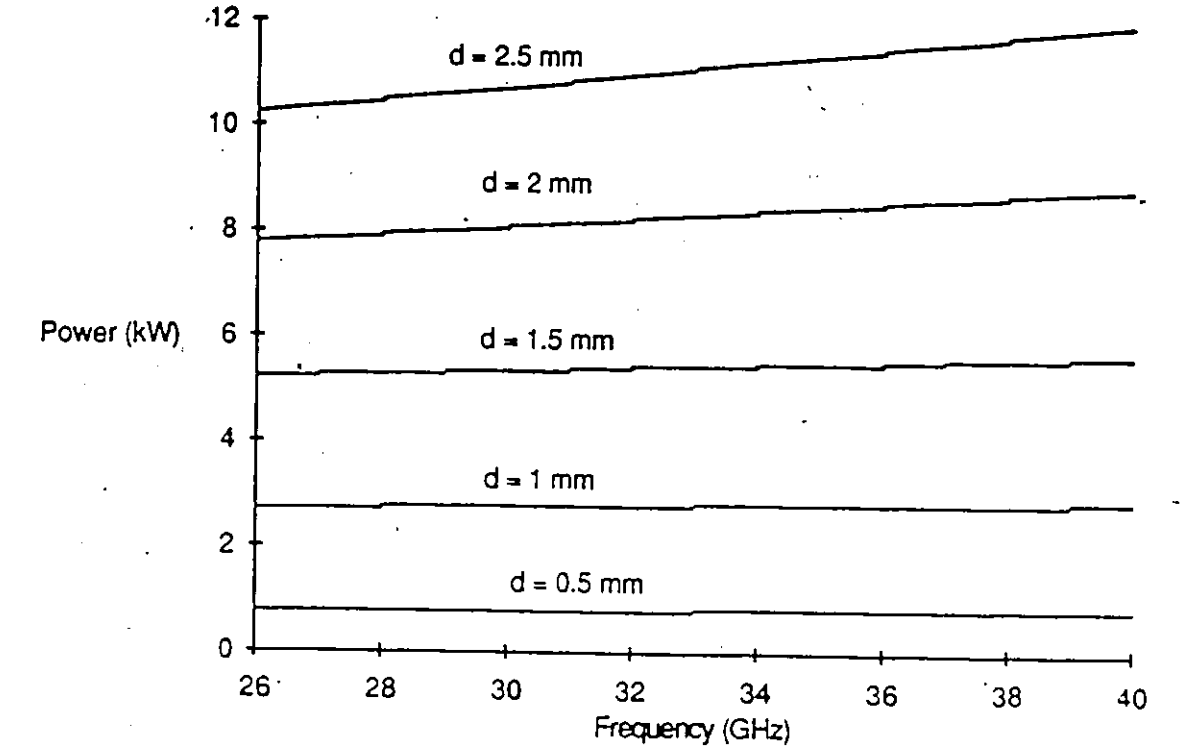

(a)

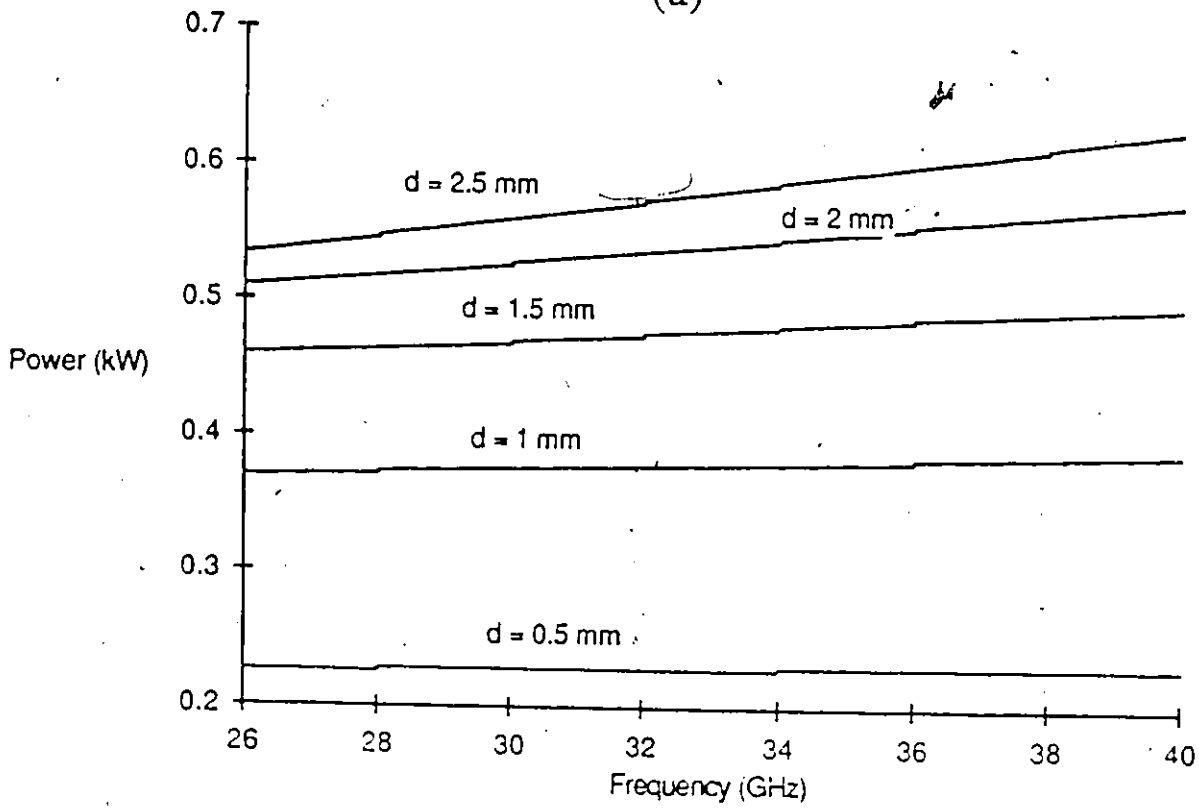

(b)

Fig.3.8 Peak power-handling capacity of WR-28 unilateral finline for different gapwidth, evaluated with (a) the FEM (b) the BEM, g=17 μm, s=254 μm, ε_r=2.22.

3.5 Discussion

By inspecting Fig. 3.5 to 3.6, one can observe that the peak power-handling of finline structures using the FEM and the BEM are quite constant over both frequency bands. Therefore, a single frequency test at any frequency within a band will be sufficient to determined the order of magnitude of the peak power-handling capacity of the line, and extend the result to the whole band. The gapwidth is also an important factor, since the maximum power that the structures can sustain decreases significantly with the gapwidth. This is true for both unilateral and bilateral finline structures. However, bilateral finlines appear to have slightly better peak power-handling capacity than unilateral finlines, in general. In Fig. 3.7a), the gapwidth of 2.5 mm is almost the height (b=3.56 mm) of the WR-28 waveguide housing. The result is not accurate because it violates the assumption that the waveguide housing have no effect on the field values in between the fins. However, the corresponding impedance values are too high for practical purposes. As a result, gapwidths largers than 1.5 mm should not be considered.

For reason explained before, the BEM gives a lower breakdown value than the FEM. However, discrepancies are so large that experimental verifications are necessary to evaluate which method yields the most accurate predictions.

Chapter 4

THEORETICAL STUDY OF THE BREAKDOWN FIELD IN SLOT-TYPE STRUCTURES

The electrical breakdown of a gas is the transition from an insulating to an almost completely conducting state. The pioneering work of Townsend [14] several years ago, defined a criterion that allows a quantitative description of breakdown. It was originally intended for direct current discharges but has been immensely useful for AC discharges of any frequency including microwave and millimeter-wave regions. Herlin and Brown [19] clearly demonstrated the relevance of the Townsend criterion to microwave breakdown, as far as basic processes in high frequency discharges are concerned.

In the case of high frequency fields, due to the periodic reversal of the field, the direction of motion of the electron cloud is reversed and an avalanche continues to build up since there is a drift motion in each direction due to the effect of collisions. In a gas discharge, the electrons are produced by ionization. The losses are due to diffusion, attachment, recombination etc. For a production rate very slightly greater than the loss rate, breakdown occurs due to the rapid increase of electrons. For suitable conditions of oscillation frequency, finline gap width, and gas pressure, we do not have a continuous unidirectional drift of electrons to the anode. This is precisely the reason why the mechanism of high frequency breakdown is simpler than that of static field breakdown. Indeed, there is no necessity for the action of secondary processes to replace the primary electrons lost to the electrodes [17].

4.1 Diffusion length

Whenever a gradient in either particle concentration or velocity exists in a gas, there will be a flow of particles in a direction which tends to reduce the gradient. This

flow is called diffusion, and will be the dominant loss mechanism in the applications considered here.

For an ionization rate per electron ν_i, which is independent of time, the electron concentration n is of the form [18]:

$$n = n_o \exp\left\{(\nu_i - D/\Lambda^2)t\right\}. \tag{4.1}$$

Here, D is the diffusion coefficient and Λ is the characteristic diffusion length having eigenvalues typical of the geometry. Also, for an ionization rate independent of spatial variation,

$$\nabla^2 n = -\frac{\gamma n}{D}, \tag{4.2}$$

where,

$$\frac{\gamma}{D} = \frac{1}{\Lambda^2}. \tag{4.3}$$

Therefore, (4.1) tells us that the rate of change of electron concentration in an ionized volume, from which electrons are lost due to diffusion, depends on the difference between ionization rate and the ratio of the diffusion coefficient to the characteristic diffusion length squared. It is an important equation, which illustrates the increase of the electron concentration that leads to breakdown, and gives a criterion for breakdown fields under the relevant conditions of the problem.

The geometry of the container, in which the ionization process takes place, is an important factor that can be characterized by the diffusion length concept introduced before. In regard to this work, one shall consider only two types of geometry:

i) Right circular cylinder

Assuming zero value at the boundaries, the electron concentration is given by [18]

$$n = n_o \sin\left(\frac{\pi z}{L}\right) J_0\left(2.405\,\frac{r}{R}\right). \tag{4.4}$$

where L is the height, R the radius of the cylinder and J_0 is the Bessel function of order zero. The eigenvalues are defined by

$$\left(\frac{2.405}{R}\right)^2 + \left(\frac{\pi}{L}\right)^2 = \frac{\gamma}{D} = \frac{1}{\Lambda^2}, \tag{4.5}$$

ii) Parallelopiped

For two parallel plates of width Y, length Z and separated by X, the electron concentration has a solution of the form [18]:

$$n = n_0 \sin\frac{\pi x}{X} \sin\frac{\pi y}{Y} \sin\frac{\pi z}{Z} . \tag{4.6}$$

The eigenvalues are defined by

$$\left(\frac{\pi}{X}\right)^2 + \left(\frac{\pi}{Y}\right)^2 + \left(\frac{\pi}{Z}\right)^2 = \frac{\gamma}{D} = \frac{1}{\Lambda^2} . \tag{4.7}$$

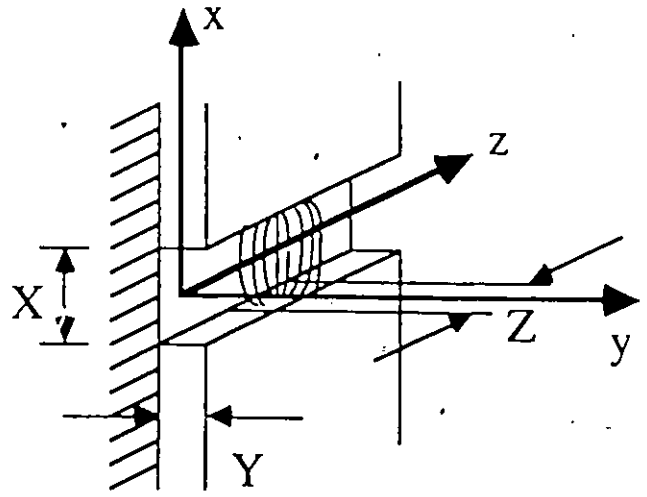

Fig.4.1 Parallelopiped container in the case of a finline structure

The relevant geometrical parameters are illustrated in Fig 4.1, in the case of a finline structure. The field is highly concentrated in between the fins where, in first

approximation, breakdown may occur. The length Z is theoretically infinite. Although, in practical situations, breakdown does not occur along the whole structure, due to the irregularities of the gapwidth. The electron diffusion takes place almost completely toward the top and bottom walls since the two opposite sides of the cavity (i.e. the conducting strips) are close for practical values of characteristic impedance. In such a case, the diffusion length depends crucially on the smaller dimensions. The breakdown can be considered to occur in a uniform field since the region where the field is concentrated is very small. However, this simple assumption must be modified for certain profiles at high frequencies. The deviation from uniformity can be treated by the definition of a characteristic diffusion length relevant under the experimental conditions. Such an approach would also be feasible for a combination of a DC magnetic or electric field with AC electric fields.

4.2 Influence of frequency and effective field concept

In the present problem, at high frequencies and with sufficiently large amplitude of the electric field, the electrons can be swept completely across the tube and collide with the walls during a half cycle. For an electric field of the form:

$$E = E_p \sin \omega t \,, \tag{4.8}$$

where $\omega = 2\pi f$ is the angular frequency, one has the following interesting relation for the breakdown field E_B in the oscillation amplitude limit [18]:

$$E_B = 2\pi \cdot 10^5 \cdot \frac{p}{\lambda} \cdot \Lambda \,, \tag{4.9}$$

where p is the pressure and $\lambda = c/f$ the wavelength.

Equation (4.9) suggests a linear relation between E and the frequency f. Breakdown values in the X-band, for example, can be calculated at given p and f by this formula.

It certainly would be tempting to extrapolate (4.9) to higher field frequencies beyond the X-band. Such a procedure would only give an extremely crude indication

of E for higher frequencies. Indeed, the transfer of energy from the electric field to the electrons becomes less efficient as the frequency increases. The inertia of the electrons results in an out-of-phase component. The energy transfer efficiency may be expressed through an effective field E_e [20], that takes into account the collision frequency :

$$E_e = E \Big/ \sqrt{2\left(1 + \frac{\omega^2}{\nu_{eff}^2}\right)}\,. \tag{4.10}$$

A theoretical analysis making use of the effective field concept has correlated all the breakdown data for air. The form of the correlation is such that it makes possible accurate predictions of breakdown fields for both continuous wave (CW) and pulsed conditions over a wide range of the experimental variables [18]. It is also reasonable to make meaningful extrapolations to nearby neighboring physical regions for which experimental data are not available. The predictions are claimed with reasonable certainty for frequencies upto 100 GHz over pressure ranges corresponding to an altitude variation from ground level to about 100 km [18]. With the use of the effective field concept, predictions can be extended up to 140 GHz. Following Lupan [21], the following relation can be used, for example, for frequencies above 25 GHz:

$$\frac{\nu_i}{p} = 2.5 \cdot 10^7 \left\{1.45(E_e/p)^{1/2} + 0.01(E_e/p)^{3/2}\right\} \exp\left(\frac{-278}{E_e/p}\right) \ \mathrm{sec}^{-1}\,\mathrm{Torr}^{-1}\,, \tag{4.11}$$

where ν_i is the average ionization rate of the heavy particles in air, E_e is the effective field and p is the pressure. The amplitude of the microwave electric field E can then be calculated using (4.10), where the effective electron collision frequency is $\nu_{eff} = 5.3 \times 10^9 p\,[\mathrm{Hz}]$. For instance, Fig. 4.2 shows the electric field breakdown values as a function of the frequency, for atmospheric pressure ($p = 760\,\mathrm{mm}$) and for ionization rates in the range $10^7 < \nu_i < 9 \times 10^9\,\mathrm{Hz}$.

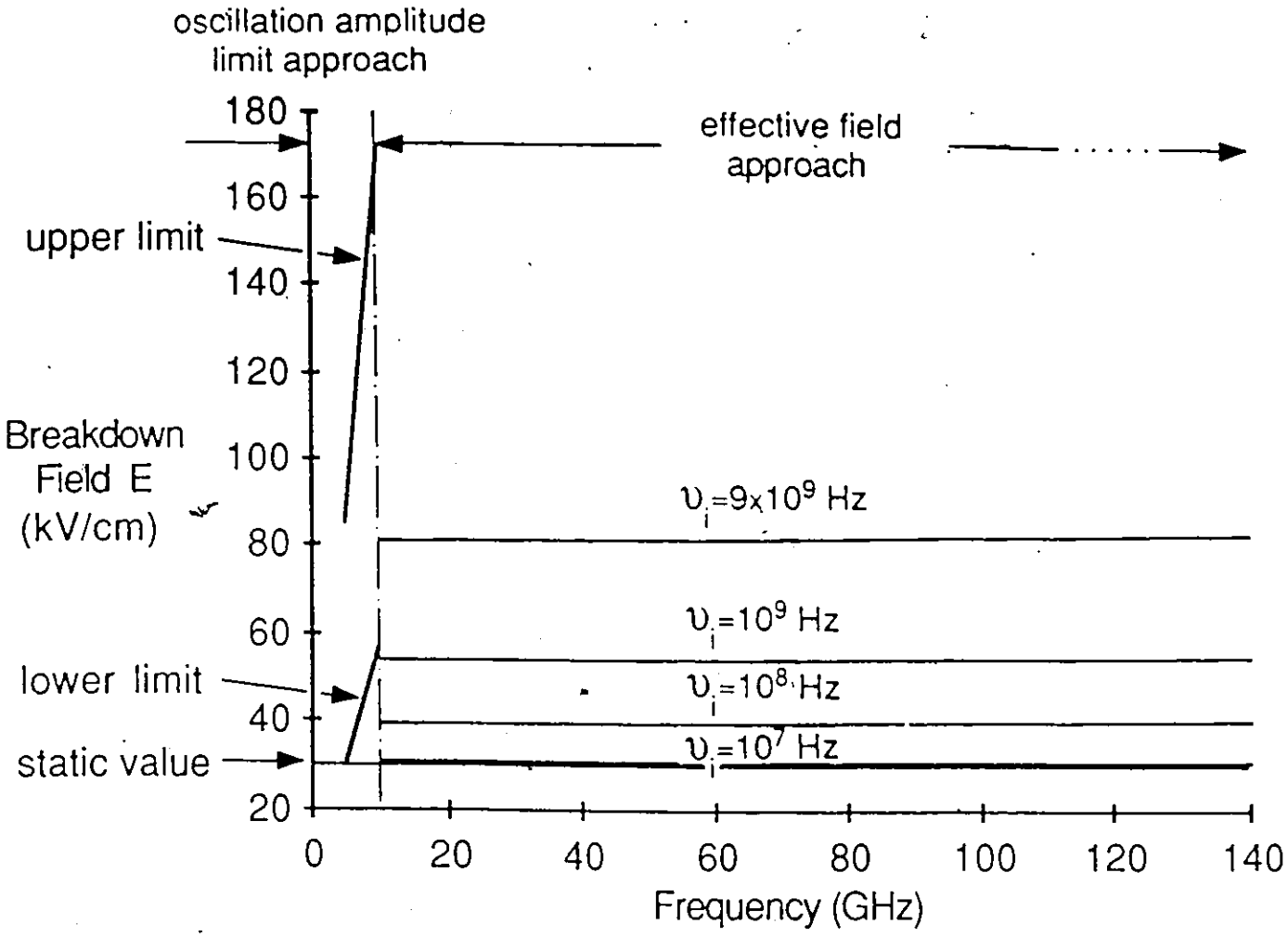

Fig.4.2 Breakdown field values in the air vs frequency (theoretical prediction). Pressure p=760 mmHg. υ_i=ionization rate. The curves in the oscillation amplitude limit approach have been evaluated in the configuration given in Fig.4.1. The curves in the effective field approach range have been obtained from [15].

As the frequency increases beyond the X-band region, the breakdown field value does not increase indefinitely, but saturates to a value, which depends on the ionization rate. In the X-band region, the oscillation amplitude limit depends on the geometry through the parameter Λ. The lower limit corresponds to the realistic case where, due to the irregularities of the gapwidth, the breakdown occurs only over a region as small as the irregularities. On the other hand, the upper limit indicates the ideal case of a breakdown occuring over an infinitely long line.

An alternative approach is that of MacDonald et al. [25], who studied the variation of D_p with E_e/p to arrive at the following representation:

$$D_p = (29 + 0.9E_e/p) \cdot 10^4 \ \text{cm}^2\,\text{Torr}\,\text{sec}^{-1}. \tag{4.12}$$

The value of D_p was calculated assuming a known variation of D_p with the average electron energy u_{ave}, in order to determine E_e for a given pressure p. This method gives values of E_e in reasonable agreement with those obtained from (4.11). D_p can also be calculated from ionization rates within a given range and for given p [18].

Measurements of pulsed breakdown fields are subject to more uncertainty because the shape, length of pulse and repetition rate all have a bearing on the result. The pulsed breakdown fields is about 10% higher as the one of CW fields for typical operations at microwave frequencies.

4.3 Superimposed DC and AC Fields

The superposition of DC and AC electric fields arises when biasing of solid state devices is needed. Ionization triggering can be made more difficult by the superimposition of a dc electric field. The modified diffusion length Λ_{DC} for superimposed fields is [18],

$$\frac{1}{\Lambda_{DC}^2} = \frac{1}{\Lambda^2} + \left(\frac{\mu E_{DC}}{2D}\right)^2, \tag{4.13}$$

and,

$$\frac{\nu_i}{D} = \frac{1}{\Lambda_{DC}^2}, \tag{4.14}$$

is the new breakdown condition. In (4.13), μ is the mobility, D the diffusion coefficient, E_{DC} is the applied DC electric field, and Λ_{DC} is computed from (4.5) or (4.7). The factor D/μ can be calculated from the average electron energy u_{ave}:

$$\frac{D}{\mu} = \frac{2}{3} \cdot u_{ave} = \frac{1}{3} \frac{m\nu^2}{e}, \tag{4.15}$$

for a Maxwellian velocity distribution. Once Λ_{DC} is determined, the corresponding breakdown value is calculated from (4.9) where Λ is replaced by Λ_{DC}.

4.4 Combination of DC Magnetic and AC Electric Fields

For ferrite devices, a DC magnetic field is superimposed on a high frequency AC electric field. A static magnetic field perpendicular to the AC electric field will cause a general increase of the value of the breakdown field. However, the general shape of the breakdown field frequency characteristic, (given by (4.11)) is not changed [26]. This is in agreement with the fact that increased losses result, due to lateral motion caused by the curvature of the electron orbits. The increased time is equivalent to a lengthening of the vessel.

When a magnetic field is applied to a gas along with a high- frequency electric field, the motion of the electrons is altered by addition of the acceleration due to the Lorentz force. In particular, the rate of diffusion is altered by different amounts in different directions. In situations in which the magnetic field is uniform and in one direction, for example, along the longitudinal direction, say z-axis, the diffusion length becomes, in Cartesian coordinates [31],

$$\frac{1}{\Lambda_b^2} = \left(\frac{1}{\Lambda_X^2} + \frac{1}{\Lambda_Y^2}\right) \cdot \frac{1}{1+b^2} + \frac{1}{\Lambda_Z^2}, \tag{4.16}$$

where, B is the magnetic field magnitude and

$$b^2 = \frac{\omega_b^2}{\nu_{eff}^2} = \frac{e^2 B^2}{m^2 \nu_{eff}^2}. \tag{4.17}$$

In cylindrical coordinates ,the equivalent diffusion length is given by:

$$\frac{1}{\Lambda_b^2} = \frac{1}{\Lambda_r^2} \cdot \frac{\nu_{eff}^2}{\nu_{eff}^2 + \omega_b^2} + \frac{1}{\Lambda_Z^2}, \tag{4.18}$$

for a magnetic field parallel to the axis of the cylinder. The effect of the magnetic field is equivalent to enlarging the container by the factor $\sqrt{1 + \omega_b^2/\nu_{eff}^2}$ in the directions perpendicular to the magnetic field. An increase in the breakdown field value is also possible due to the effective rise of pressure, when a magnetic field is superimposed on a low frequency electric field. Once Λ is computed, the breakdown value of the field is computed with (4.9) where Λ is replaced by Λ_b. However, for appreciable values of the magnetic field which imply a relatively great Lorentz force, one has to study carefully an expansion of the Boltzmann transport equation in spherical harmonics in space, and in Fourier series in time. The resulting differential equation for the distribution function can be integrated to determine electrical breakdown values [31].

The effects of pressure and altitude on breakdown have become important due to problems of transmission at high altitude and with the increasing interest in studies of breakdown in the atmosphere. The problems in the investigations on the ionized shock region in the neighborhood of missiles also require a sound knowledge of the effects of pressure and altitude on breakdown. In the case of air, the breakdown field initially falls with the increase in altitude and then rises again like a parabola [18].

Chapter 5

EXPERIMENTAL PROCEDURE & RESULTS

5.1 Introduction

An experimental procedure was conducted in order to determine the peak power-handling capacity of finline structures. First, the experiments were conducted at 9.6 GHz, with unilateral finlines of different gapwidths.

5.2 High Frequency Case (X-Band)

Finlines with gapwidth of 0.5 to 2.5 mm were prepared, and mounted in a WR-90 waveguide. Thirty four-μm thickness fins were etched on a 762-μm thick dielectric substrate (R-T duroid, $\varepsilon_r = 2.22$). Transitions from finline to waveguide consisted of single exponentially tapered conducting strips [11]. Quarter-wave stubs were cut in the dielectric substrate [12] in order to match it with respect to the empty waveguide (see Fig. 5.1).

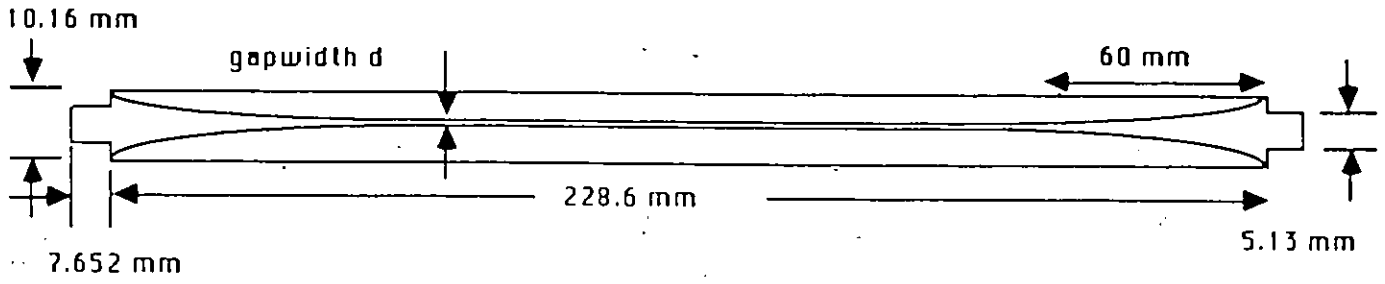

Fig. 5.1 Finline sample used for experimental procedures at high frequency.

The block diagram of the measurement system is shown in Fig. 5.2. A radar station which transmitted a 0.8 – μs pulse width signals, with a repetition rate of 1000 pulse/sec was used. The generator (magnetron) could produce a maximum peak power of 300 kW at 9.6 GHz. A built-in circulator and teflon window prevented damages due to reflections. In order to read the transmitted power level, a power-meter was connected in front of the test unit. An oscilloscope was connected, through a detector, at the end of the unit in order to observe any sudden change of the signal when the breakdown occured.

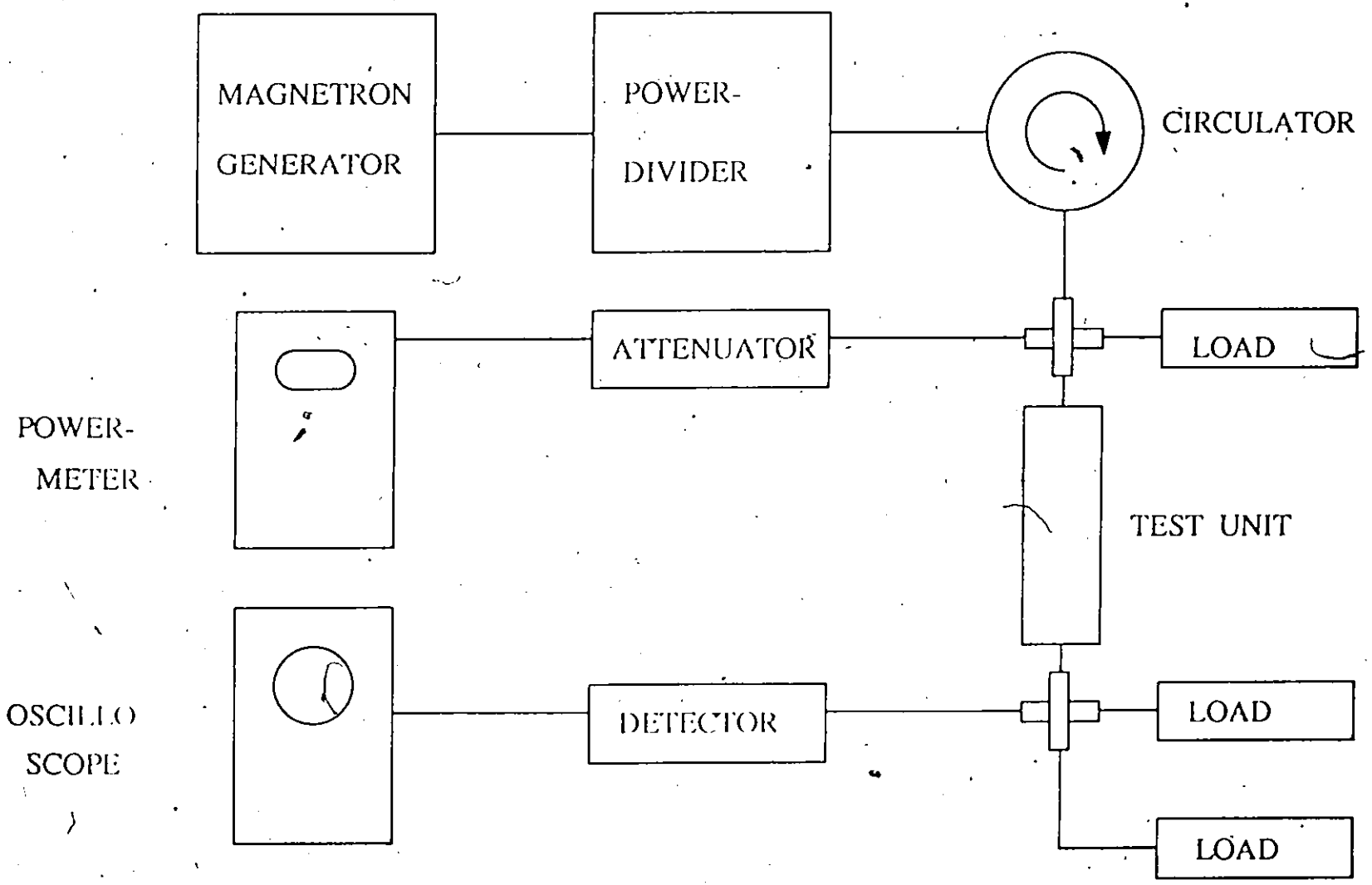

Fig.5.2 Experimental set-up for maximum peak power measurements at 9.6 GHz.

As a first result, experiments confirmed that the breakdown did occur in the gap before any damage of the dielectric substrate, or of the conducting strips, due to the dissipations. In order to test the accuracy of both theoretical methods, experiments were conducted at extremely low frequency (60 Hz) with a high voltage generator. Hence, a static condition of operation was practical realized. Table 5.1 shows the peak power levels at which breakdown occured in the structure for different gapwidths. Two trials were made in each case, and the average value was taken for comparison with the theoretical results. As expected, the peak power required for a breakdown situation, increases as the gapwidth increases.

d(mm)	1st trial(kW)	2nd trial(kW)	Average(kW)
0.5	5.595	5.425	5.510
1.0	9.500	8.375	8.938
1.5	10.75	10.75	10.75
2.0	12.00	11.50	11.75
2.5	19.06	18.02	18.54

Table 5.1 Peak-power handling capacity of WR-90 waveguide housing finlines with different gapwidth at 9.6 GHz(X-band). Repetition of pulse is 1000 pulses/sec with pulse duration of 0.8 μsec. Conductor thickness g=34 μm and substrate thickness s=762 μm.

It was observed on the oscilloscope that when breakdown occurred, there was a drop of approximately 10% in amplitude of the transmitted pulses. This corresponds to a drop of 20% in terms of peak power. As expected, larger gapwidths could sustain more power. After the experiments, marks due to air breakdown could be clearly seen

on the dielectric surface of the samples in between the fins, as sketched in Fig 5.3a.

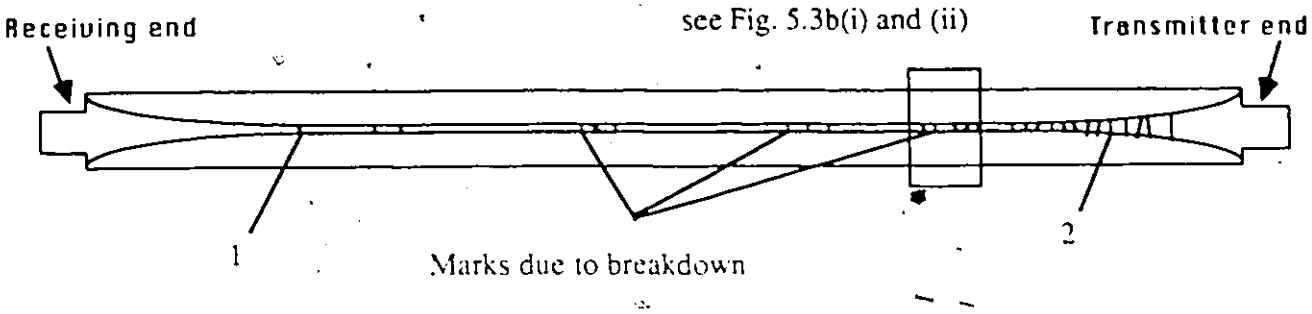

Fig.5.3a Sketch of a finline sample after experiment, illustrating propagation of breakdown.

One can deduce that breakdown seems to occur first at the receiving end (region 1), then, because of the increase of field strength due to reflections, it propagates back to the transmitter end (region 2). The propagation stops beyond the point where the gapwidth is large enough to produce a field strength below that required for the breakdown condition.

The electron micrography of Fig. 5.3b(i) shows that these marks correspond to the locations where the breakdown occurred. It is interesting to note that these locations correspond to where the irregularities of the profile make the gap narrower.

It is also worth to notice that the breakdown did not occur on the full length of the line because of these irregularities. This has an important impact on the evaluation of the field breakdown value in dynamic conditions. A magnified version of Fig. 5.3b(i) is shown in Fig. 5.3b(ii). It clearly shows the damages made on the structure. Melting of the dielectric surface and erosion of the conductor edges can be observed.

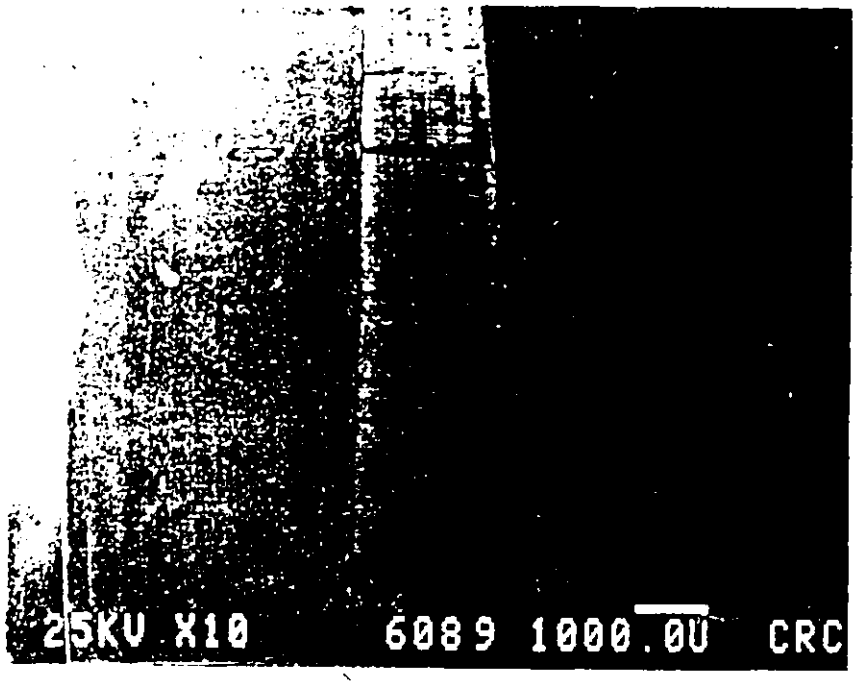

(i)

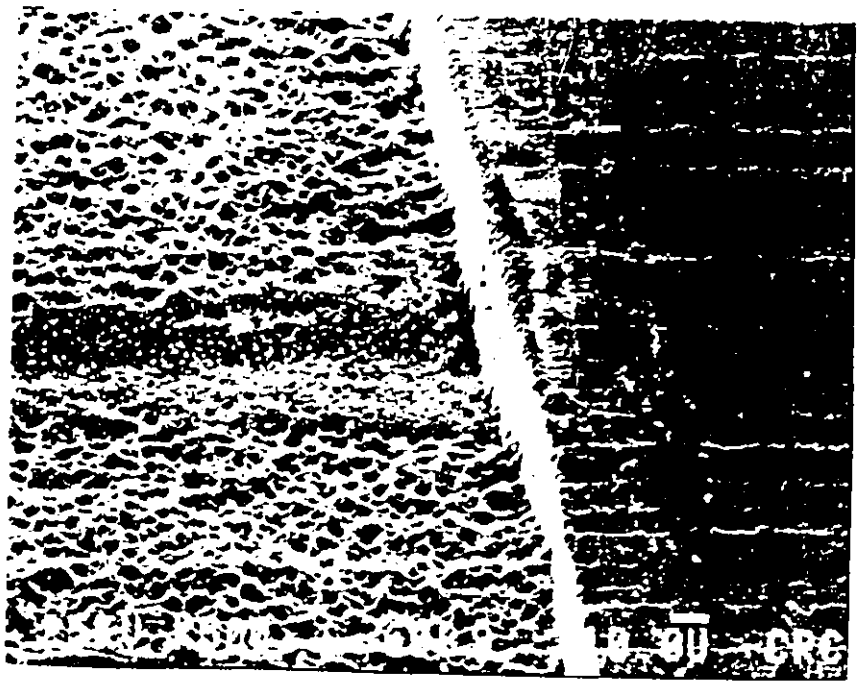

(ii) magnification of (i)

Fig.5.3b Electron Micrographs of a Finline Structure after the experiment, at the location indicated in Fig. 5.3a.

5.3 Quasi-static experiment (60Hz)

The theoretical analysis proposed in this thesis is based on a quasi-static approach. In order to test the accuracy of the two methods used for field computations, it was necessary to perform experimental tests in a DC condition. Because no high voltage DC generator was available, experiments were performed at 60 Hz. In terms of field distribution, one practically deals with the static situation. Finline samples were the same as the ones illustrated by Fig 5.1, except that the dielectric stubs were not inserted. The preparations of the samples were the same as described in section 5.2. The experimental setup is displayed in Fig. 5.4. The high-voltage generator could produce voltage levels up to 30 kV at 60 Hz. In order to avoid breakdown between the two copper connectors, they were located at both extremities of the sample.

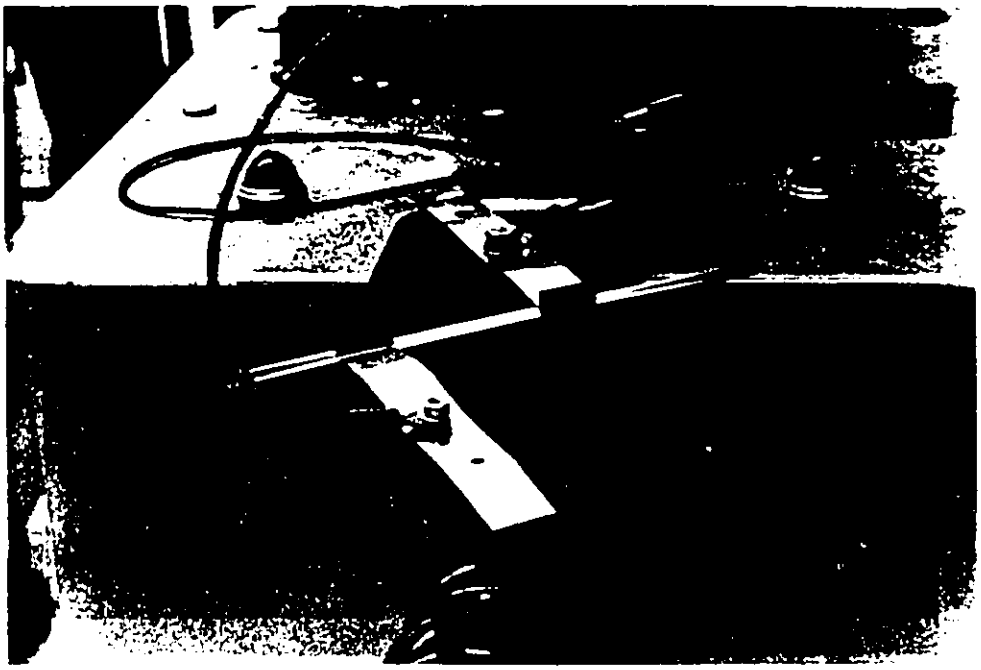

Fig.5.4 Experimental set-up for quasi-static experiment (60Hz).

Fig.5.5 Air breakdown occuring in a unilateral finline substrate, at 60 Hz.

The breakdown voltage values are shown in Table 5.2, for different gapwidths. Like in the high frequency case, the required voltage for a breakdown situation, increases as the gapwidth increases.

d(mm)	1st trial(kV)	2nd trial(kV)	Average(kV)
0.5	1.061	------	1.061
1.0	1.838	------	1.838
1.5	2.546	2.970	2.758

Table 5.2 Peak breakdown voltage of unilateral finline substrates for different gapwidths at 60 Hz.

Sparks between the two conductors could be clearly seen when the breakdown occured (see Fig. 5.5). The voltage was decreased after the first spark and then increased again, in order to observe if the same voltage led to the same breakdown voltage value. Usually, a higher breakdown voltage value was obtained because of some physical and geometrical modification of the edge profile by the previous trial.

Chapter 6

THEORY AND EXPERIMENTS: COMPARISONS AND DISCUSSIONS

From the theoretical predictions presented in Chapter 2, it was found that the two numerical methods yield discrepant results for the same stuctures. Consequently, these two methods have to be analysed and compared with the experimental results.

The 60-Hz experimental results will determine whether the BEM or the FEM is the most accurate. Then, the theoretical predictions computed with the most accurate method will be compared with the experimental results obtained at 9.6 GHz. Finally, corrections of the field breakdown value, due to the various parameters, described in Chapter 4, will be introduced in the comparisons.

6.1 Low Frequency Analysis

Table 6.1 compares the theoretical values of the voltage at which breakdown occurs, with the experimental results.

d(mm)	Expt(kV)	FEM(kV)	%error	BEM(kV)	%error
0.5	1.061	0.715	32.6	0.261	75.4
1.0	1.838	1.288	29.9	0.383	79.2
1.5	2.758	1.765	36.0	0.475	82.8

Table 6.1 Comparison between experimental and theorectical results obtained for low frequency breakdown (60Hz).

Although, an error of about 30% occurs with the FEM computations, these are

about 3 times as close to the experimental results, as those given by the BEM. This error of around 30% cannot be explained by the absence of the enclosure. Indeed, for such gapwidths, it has been verified that the enclosue has very little effect on the values in the region of interest. However, these discrepancies with experimental data could come from irregularities of the strip profile. Also, at least 10% error was produced by the build-in voltmeter of the generator.

The large errors produced by the BEM cannot be explained. For observation points at remote locations from the conductor edges, the field values compare with those given by the FEM. However, large discrepancies occured for observation points close to the conducting edges. Presently, it is not possible to say whether the errors are inherent to the BEM or to the available program. Unfortunately, no access to the code was possible in order to investigate the source of error. As a result, the BEM will not be used for theoretical prediction at high frequency.

6.2 High Frequency Analysis

In chapter 3, diagrams of Fig. 3.5-3.8 were established by assuming a static breakdown field value of 30 kV/cm in the air at atmospheric pressure. Corrections due to the geometry and the frequency can be made, by using the diagram shown in Fig. 4.2. For instance, for an ionization rate of 10^{-8} Hz, the maximum admissible field value would be multiplied by 1.8 and, consequently, the power would by increased by a factor 3.4. For the end of the X-band region, since it is at the limit of both approaches, the correction factor can be evaluated by the effective field approach or, if ν_i is not known, by the oscillation amplitude limit. Table 6.2 gives the comparison between the theoretical predictions and the experimental results at 9.6 GHz.

d(mm)	FEM(kW) lower limit	Expt(kW)	%error	FEM(kW) upper limit
0.5	2.125	5.510	61.4	49.95
1.0	5.349	8.938	40.2	125.7
1.5	8.830	10.75	17.9	207.6
2.0	11.76	11.75	00.0	276.4
2.5	14.25	18.54	23.1	335.0

Table 6.2 Comparison between theoretical and experimental results for unilateral finline structures at 9.6 GHz. WR-90 waveguide is used with conductor thickness g=34 μm and dielectric thickness s=762 μm.

The upper and lower limits are computed with (4.9) with the extreme values of the diffusion length Λ ($p = 760-$mm Hg). The upper limit corresponds to $Z = \infty$ in

(4.7). This assumes that breakdown occurs along the entire longitudinal region, i.e. along the Z-axis. This is not realistic since the profiles show some irregularities. Observations of the samples after experimental tests showed that, indeed, breakdown occurs only over a length of the order of magnitude of size of the irregularities (see Fig. 5.3(b)ii). Taking $Z_{min} = 12\mu$m (see Fig. 4.1 p. 45), one obtains the lower limit values shown in table 4.2. One observes that experimental values are within the predicted range of values but very close to the lower bound which corroborates the assertion about the value of the diffusion length.

From table 6.2, great errors occurred for small gapwidths. This can be explained by the error introduced by the impedance calculation using the SDM and the evaluation of the diffusion length. The parallelopipe geometry of the breakdown path along the longitudinal direction is assumed to be constant for different gapwidths, a better approximation would be to modify the length Z accordingly with the gapwidth d. Nevertheless, all experimental results fall within the predicted range, given by the upper and lower limits of the diffusion length.

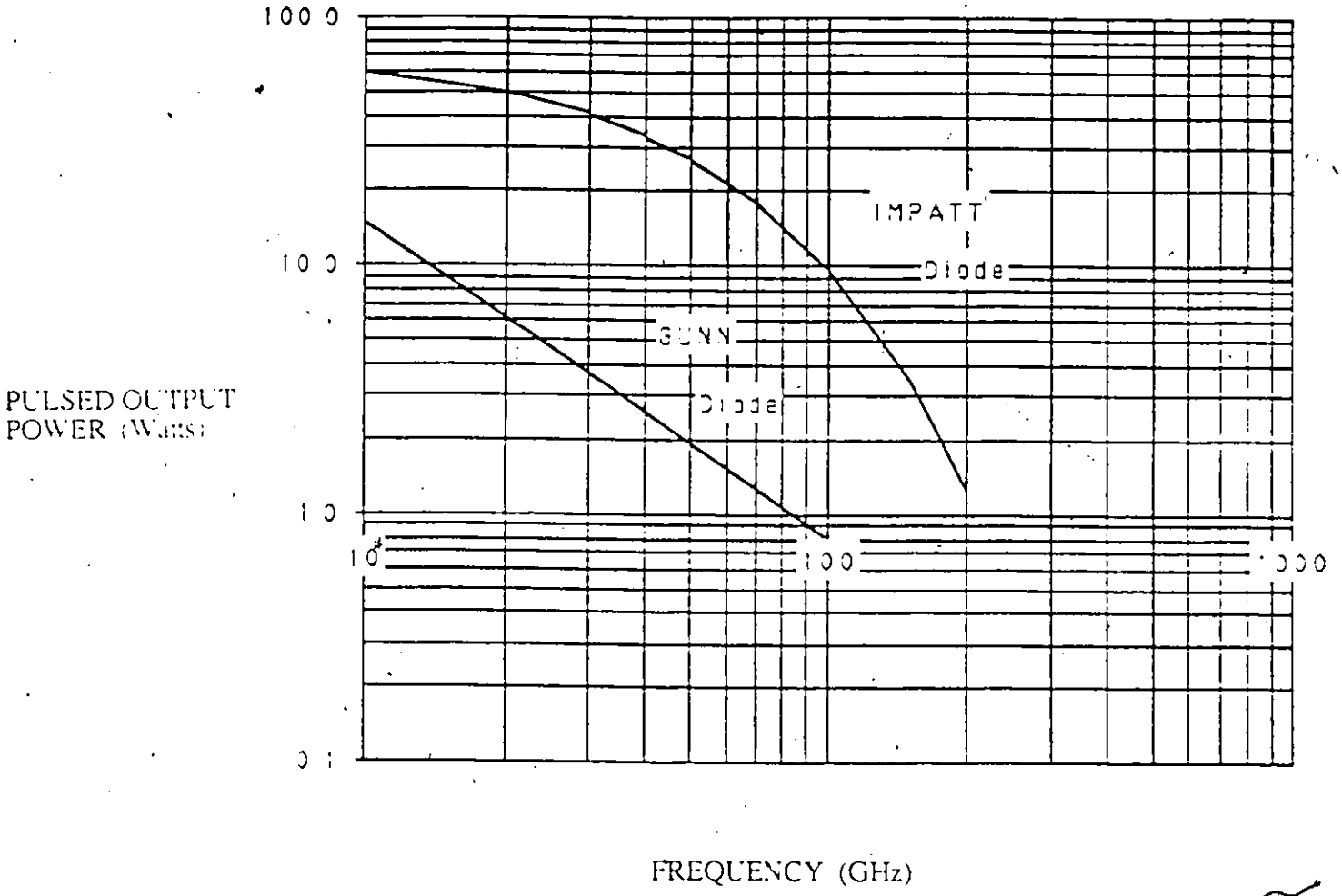

Fig.6.1 State of the art for millimeter wave solid state sources[1].

6.3 Discussion

An interesting fact arises from the experiments, i.e. the finline structures actually can sustain quite high peak power levels, up to the kilowatt range.

Fig. 6.1 shows that, presently solid state sources can generate peak-power levels much below the kilowatt range. As compared to the empty waveguide the peak power-handling capacity is reduced by two orders of magnitude.

Maximum power (kW)	Finline		Empty waveguide
	unilateral	bilateral	
WR-28	2.3	3.0	128.2
WR-90	4.5	4.5	1160.

Table 6.3 Comparison of the maximum peak power-handling capacity of finlines (gapwidth=1 mm) with the corresponding waveguide structures. Finline dimensions as in Table 3.3 (ε_r=2.22).

Table 6.3 shows the maximum transmissible peak power of finlines structures ($d = 1$ mm), compared with the corresponding empty waveguide structure (maximum value in the band). The theoretical predictions indicate that, as expected, the peak power-handling capacity of an empty waveguide is severely affected by the introduction of the finline substrate. Hence, there is some concern when finline structures are fed with tubes, which can generate hundreds of kilowatts in pulsed operation.

Chapter 7
CONCLUSION

In this thesis, theoretical and experimental results pertaining to the maximum peak power values that finline structures can transmit, before breakdown occurs, are presented and discussed. A quasi-static approach is proposed to evaluate the field configuration in various structures. Theoretical corrections to the static breakdown value in the air are proposed, enabling extrapolations at higher frequencies up to 140 GHz.

Both the FEM and the BEM were compared with experimental results performed at 9.6 GHz and at 60 Hz. The low-frequency experiments allowed one to select the most accurate method to compute the field distribution. It turned out, that the FEM was the most accurate method for these types of structure, when very thin subregions were used.

The dynamic breakdown mechanism was investigated, and guidelines for extrapolation of the breakdown field values up to 140 GHz is proposed. For instance, the breakdown field value increases with the frequency of the applied field. However, at frequency above 10 GHz this value tends to saturate. The study also includes the situations in which a static field is produced, for instance, by biasing of solid state devices, and superimposed on a high frequency field.

The experimental observations showed that breakdown occurs only in a very small location within the gap between the conductors. This is due to the irregularities of the conducting strip profile.

Simulations showed that the peak power-handling capacity of finlines is more than two orders of magnitude below the one of an empty waveguide. However, that level is about ten times larger than the present state of the art concerning the output power levels that solid state devices, (which are commonly used with E-plane structures) can generate.

Appendix

COMPUTER PROGRAM LISTING

This appendix contains listing of the computer program, the Finite Element Method, which was used in this thesis. Data for unilateral as well as bilateral finline structures are given.

FINITE ELEMENT METHOD (FEM)

```
C
C To evaluate maximum electric field of bilateral and
C unilateral finline structures using the Finite Element
C Method.
C
C Program provided by Dr.  G.I. Costache.
C
C
C
C Input data for bilateral and unilateral finline structures
C a=22.86 mm, b=11.43 mm, d=0.5 mm, s=0.762 mm, g=0.034 mm.
C
C
  implicit real*8 (a-h,o-z)
  dimension nv1(100),nv2(100),nv3(100),p(72),eps(100)
  dimension a(99,99),b(99)
  dimension f(3,3),s(3),x(72),y(72),iv(100,3)
C
C p(i)-potential of node (vertice) "i".
C Set Dirichlet nodes to their assigned potentials
C and Neumann and unknown nodes to zero potential.
C
  data p/17*0.0,11*1.0,44*0./
C
C eps(i)-dielectric constant of triangle "i".
C
  data eps/20*2.22,80*1./
C
C Coordinates (x(i),y(i)) represent the location of
C the node point "i".
C
  data x/8*415.,414.,398.,7*381.,0.,381.,1558.,3301.,5043.,
 *6205.,5*11430.,2*7656.,7366.,7075.,8817.,6205.,8817.,4172.,
 *2429.,977.,1558.,2139.,3301.,3591.,4172.,2*4463.,2720.,
 *1558.,10*0.,3*381.,977.,1267.,2139.,2*2429.,2720.,1558.,
 *2*1267.,977.,416.,398./
  data y/0.,1071.,2142.,3213.,4284.,4820.,4829.,4*4830.,
 *4820.,4284.,3213.,2142.,1071.,0.,7*5080.,4820.,3213.,1607.,
 *2*0.,1071.,2142.,3213.,4017.,4820.,4955.,4980.,5005.,5030.,
 *4955.,4930.,4820.,3749.,2678.,1071.,4*0.,536.,1607.,2678.,
 *3749.,4284.,4820.,4905.,4980.,2*5030.,4980.,4930.,4905.,
 *4880.,4284.,3213.,2142.,536.,1607.,2678.,3749.,4820.,4831.,
 *4880./
C
C Each node (vertice) is assigned a number beginning
C with the Dirichlet nodes.
C nv1(i), nv2(i), nv3(i) represent the three vertice
C code numbers of the three vertices of triangle "i".
C
  data nv1/17,2*16,2*15,2*14,2*13,2*12,2*11,2*60,59,3*58,57,
```

```
+38,20,3*37,21,22,23,4*35,25,3*33,3*31,27,28,29,45,44,43,3*32,
+42,41,40,3*37,39,3*59,39,40,3*63,41,42,43,7*66,67,68,69,3*63,
+70,71,72,60,11,10,9,8,4*71,6,5,4,3*68,3,2,1/
  data nv2/2*49,2*50,2*51,2*52,2*53,2*54,2*55,3*56,57,4*19,
+20,21,3*36,22,23,24,25,3*34,32,2*26,27,6*30,44,43,42,3*34,
+41,40,39,3*38,60,2*61,39,40,41,3*64,42,43,44,45,46,47,67,3*65,
+68,69,70,3*62,71,6*72,8,7,6,5,3*69,4,3,2,2*47/
  data nv3/48,17,49,16,50,15,51,14,52,13,53,12,54,11,55,60,59,
+56,57,18,58,2*38,20,21,22,3*34,23,24,25,33,32,26,25,32,26,27,
+28,29,45,44,3*31,43,42,41,3*36,40,39,59,58,61,39,3*62,40,41,
+42,3*65,43,44,45,46,47,67,68,3*64,69,70,71,3*61,60,11,10,9,8,
+7,6,3*70,5,4,3,3*67,2/
C
C Part I-main program
C
C Function q used in evaluating the S matrix
C
  q(x1,y1,x2,y2,x3,y3)=x1*y2-x2*y1+x2*y3-x3*y2+x3*y1-x1*y3
C
C File 6 and 7 are the output files,
C
  open(6,file='bilateral.out',status='new')
  open(7,file='bilateral.dat',status='new')
C
C noptl - total number of nodes
C ndir - total number of nodes with Dirichlet values.
C notr - total number of triangles
  noptl=72
  ndir=28
  notr=100
C
C
C Input data for unilateral finline structure
C
C
  dimension nv1(165),nv2(165),nv3(165),p(105),eps(165)
  dimension a(164,164),b(164)
  dimension f(3,3),s(3),x(105),y(105),iv(165,3)
  data p/15*0.0,19*1.0,71*0./
  data eps/143*1.,20*2.22,2*1./
  data x/6*11447.,11447.,11446.,11421.5,6*11413.,5*0.,6016.,8422.,
+9625.,10651.,11413.,12633.,14438.,16243.,17747.,5*22860.,4*11413.,
+10*10651.,11421.5,11448.,12032.,12332.,3*12633.,3*13836.,
+13536.,13235.,12332.,12032.,12633.,13235.,14438.,14739.,
+15340.,2*15641.,19251.,2*18950.,18348.,20454.,17747.,20454.,
+15340.,13536.,12032.,9926.,9625.,3*9324.,2*8121.,8422.,
+8723.,9024.,9625.,9024.,8121.,2*7219.,2*6918.,3609.,2*3910.,
+4211.,5113.,2406.,2707.,7821.,9324./
  data y/0.,1071.,2142.,3213.,4284.,4829.,4830.,3*4830.,
+4284.,3213.,2142.,1071.,2*0.,1607.,3213.,4820.,11*5080.,4820.,
+3213.,1607.,0.,4855.,4930.,4980.,5030.,0.,536.,1607.,2678.,
+3749.,4284.,4820.,4905.,4980.,5030.,4880.,4831.,4820.,3749.,
+2678.,1607.,2*0.,536.,2142.,3213.,4284.,4880.,4905.,4955.,
```

```
     +4930.,4820.,3749.,2678.,1071.,2*0.,1071.,2142.,3213.,4017.,
     +4820.,4955.,4980.,5005.,5030.,4284.,3213.,2142.,1071.,2*0.,
     +1607.,2678.,3749.,4552.,4880.,4930.,4820.,3213.,2142.,1071.,
     +2*0.,1071.,2142.,3213.,4820.,4017.,4955.,4980.,5005./
       data nv1/1,2,3,3*51,4,5,6,3*48,7,8,3*47,48,49,3*58,50,51,
     +52,7*55,56,57,3*63,58,59,60,3*35,61,3*76,62,63,64,3*71,
     +65,66,67,68,32,31,3*70,30,29,71,73,4*74,27,26,25,3*76,24,
     +23,3*38,39,40,3*79,41,42,88,87,78,3*86,79,80,81,4*83,84,
     +85,4*91,87,88,44,3*45,103,2*102,90,91,92,3*97,93,94,95,14,
     +15,16,2*98,99,16,17,4*101,19,20,3*103,21,22,23,36,35,34,3*44,
     +33,8,9,3*41,10,11,12,3*38,0,0/
       data nv2/2*53,2,3,4,3*50,5,6,7,2*47,7,34,60,48,3*59,49,
     +50,51,3*56,52,53,54,67,66,2*65,56,57,58,3*62,59,60,34,3*77,
     +61,62,63,3*73,64,65,66,6*69,31,30,4*72,73,29,28,27,26,3*75,
     +25,24,23,36,82,81,39,3*80,40,41,42,4*43,78,79,3*85,80,81,82,
     +93,84,3*92,85,86,87,4*89,46,103,102,90,3*99,91,92,93,6*96,
     +15,16,4*100,17,18,19,2*99,19,20,21,5*46,36,35,34,33,3*43,
     +8,9,10,3*40,11,12,13,37,0,0/
       data nv3/2,3*52,3,4,5,3*49,6,7,3*33,34,2*60,48,49,50,3*57,
     +51,52,53,54,67,66,65,56,3*64,57,58,59,3*61,60,36,35,61,62,
     +3*75,63,64,65,3*70,66,67,68,32,31,30,2*71,30,73,2*29,28,27,
     +3*73,26,25,24,3*77,37,82,2*81,39,40,41,3*78,44,88,2*87,78,
     +79,80,3*84,81,94,2*93,84,85,86,87,2*90,87,88,44,103,3*89,
     +90,91,3*98,92,93,94,95,14,15,3*97,16,98,17,2*99,17,18,19,
     +3*102,20,21,22,23,36,4*45,34,33,8,3*42,9,10,11,3*39,12,13,
     +0,0/
       q(x1,y1,x2,y2,x3,y3)=x1*y2-x2*y1+x2*y3-x3*y2+x3*y1-x1*y3
       open(6,file='unilateral.out',status='new')
       open(7,file='unilateral.dat',status='new')
       noptl=105
       ndir=34
       notr=165
     C
     C
     C
       nn=noptl-ndir
     C
     C scale is the scaling factor
     C
       accept *,scale
       pi=3.141592654
       do 1000 i=1,notr
       iv(i,1)=nv1(i)
       iv(i,2)=nv2(i)
       iv(i,3)=nv3(i)
  1000 continue
     C
     C File 7 contains all the vertices of each triangles
     C
       write(7,fmt=846)
   846 format ('MAI',/,'PD;',/,'BEGIN')
       do 847 i=1,notr
       write(7,fmt=848)x(nv1(i)),y(nv1(i))
```

```
      write(7,fmt=848)x(nv2(i)),y(nv2(i))
      write(7,fmt=848)x(nv3(i)),y(nv3(i))
      write(7,fmt=848)x(nv1(i)),y(nv1(i))
      write(7,fmt=849)
  847 continue
  848 format(2e14.6)
  849 format('W W',/,'PU;',/,'CON',/,'PD;',/,'BEGIN')
      write(7,fmt=850)
  850 format('W W',/,'PU;',/,'STO',/,'STO')
      do 6 i=1,notr-1
      b(i)=0.
      do 6 j=1,notr-1
    6 a(i,j)=0.
      do 16 itr=1,notr
      i1=iv(itr,1)
      i2=iv(itr,2)
      i3=iv(itr,3)
      det=q(x(i1),y(i1),x(i2),y(i2),x(i3),y(i3))
      det=dabs(det)
      f(1,1)=(x(i2)*y(i3)-x(i3)*y(i2))/det
      f(1,2)=(x(i3)*y(i1)-x(i1)*y(i3))/det
      f(1,3)=(x(i1)*y(i2)-x(i2)*y(i1))/det
      f(2,1)=(y(i2)-y(i3))/det
      f(2,2)=(y(i3)-y(i1))/det
      f(2,3)=(y(i1)-y(i2))/det
      f(3,1)=(x(i3)-x(i2))/det
      f(3,2)=(x(i1)-x(i3))/det
      f(3,3)=(x(i2)-x(i1))/det
      ar=dabs(det)/2.
      do 23 i=1,3
      l=iv(itr,i)-ndir
      if(iv(itr,i).le.ndir) go to 23
      do 24 k=1,3
      s(k)=ar*(f(2,k)*f(2,i)+f(3,k)*f(3,i))
      s(k)=s(k)*eps(itr)
   24 continue
      do 14 k=1,3
      if (iv(itr,k).le.ndir) go to 15
      lc=iv(itr,k)-ndir
      a(l,lc)=a(l,lc)+s(k)
   15 b(l)=b(l)-p(iv(itr,k))*s(k)
   14 continue
   23 continue
   16 continue
      do 264 i=1,notr-1
      b(i)=b(i)/scale
      do 264 j=1,notr-1
  264 a(i,j)=a(i,j)/scale
    C
    C Solve the system of equations
    C
      call sist(a,b,nn)
    C
```

```
C File 6 contains the unknown node potentials
C
  do 165 i=1,nn
  write(6,fmt=164) (i+ndir),b(i)
165 continue
164 format(' Node ',i4,' potential = ',e17.7)
  stop
  end
C
C
C Subroutine sist
C a - matrix of the system
C b - right hand side, contains solution
C n - dimension of the system
C
C
  subroutine sist(a,b,n)
  implicit real *8 (a-h,o-z)
  dimension a(99,99),b(99)
  nm1=n-1
  d=1.0
  do 7 k=1,nm1
  ba=a(k,k)
  j=k
  kp1=k+1
C
C Find max term in column
C
  do 1 i=kp1,n
  if (dabs(ba).ge.dabs(a(i,k))) go to 1
  ba=a(i,k)
  j=i
1 continue
  d=d*ba
  if(j.le.k) go to 3
  if(dabs(d).eq.0.)  go to 9
C
C Interchange rows
C
  do 2 i=k,n
  h=a(k,i)
  a(k,i)=a(j,i)/ba
2 a(j,i)=h
  h=b(k)
  b(k)=b(j)/ba
  b(j)=h
  go to 5
C
C Divide row by max coefficient
C
3 do 4 i=kp1,n
4 a(k,i)=a(k,i)/ba
  b(k)=b(k)/ba
```

```
 5 do 7 i=kp1,n
   do 6 j=kp1,n
 6 a(i,j)=a(i,j)-a(i,k)*a(k,j)
 7 b(i)=b(i)-a(i,k)*b(k)
   d=d*a(n,n)
   if(dabs(d).eq.0.)  go to 9
   b(n)=b(n)/a(n,n)
 C
 C Back substitution
 C
   do 8 i=1,nm1
   k=n-i
   kp1=k+1
   do 8 j=kp1,n
 8 b(k)=b(k)-a(k,j)*b(j)
   write (6,fmt=11)
11 format(' ok')
   return
 9 write (6,fmt=10)
10 FORMAT(' SINGULAR SOLUTION')
   return
   end
```

BIBLIOGRAPHY

[1] P. Bhartia and I. J. Bahl, "*Millimeter Wave Engineering and Applications*," John Wiley & Sons, Inc., Toronto, 1984.

[2] S. Hopfer, "The Design of Ridged Waveguides," *IRE Trans. Microwave Theory Tech.*, vol. MTT-31, pp. 20–29, Oct 1955.

[3] D. G. Jablonski, "Power-Handling Capabilities of Circular Dielectric Waveguide at Millimeter Wavelengths," *IEEE Trans. Microwave Theory Tech.*, vol. MTT-33, no. 2, pp. 85–89, Feb 1985.

[4] W. Yue and M. M. Ney, "Peak Power-Handling Capacity of Finline Structures," *IEEE-Electronicom'85 proc.*, vol. 1, pp. 140–142, 1985.

[5] Y. C. Shih, "*The Analysis of Finlines Using Transmission Line Matrix and Transverse Resonance Methods*," M. A. Sc. thesis, Univ. of Ottawa, pp. 69–73, 1980.

[6] L.-P. Schmidt and T. Itoh, "Spectral Domain Analysis of Dominant and Higher Order Modes in Fin-Lines," *IEEE Trans. Microwave Theory Tech.*, vol. MTT-28, no. 9, pp. 981–985, Sep 1980.

[7] R. Vahldieck, "Accurate Hybrid-Mode Analysis of Various Finline Configurations Including Multilayered Dielectrics, Finite Metallization Thickness, and Substrate Holding Grooves," *IEEE Tran. Microwave Theory Tech.*, vol. MTT-32, no. 11, pp. 1454–1460, Nov 1984.

[8] P. B. Jones, "Application of Transmission Line Matrix Method to Homogeneous Waveguides of Arbitrary Cross-Section," *Proc. IEEE*, vol. 119, no. 8, Aug 1972.

[9] C. A. Brebbia, "*The Boundary Element Method for Engineers*," London: Pentech Press, 1984.

[10] T. Kitszawa and R. Mittra, "Analysis of a Finline with Finite Metallization Thickness," *IEEE Trans. Microwave Theory Tech.*, vol. MTT-32, no. 11, pp. 1484–1486, Nov 1984.

[11] W. J. R. Hoefer, "*Fin Line Design Manual. I*,"

[12] C. J. Verver and W. J. R. Hoefer, "Quarter Wave Transformers for Matching Transitions between Waveguides and Fin Lines," *1984 IEEE MTT-S Intl. Microwave Symposium Digest*, pp. 417–419, San Francisco, Ca.

[13] K. Solbach, "The Status of Printed Millimeter-Wave E-Plane Circuits," *IEEE Trans. Microwave Theory Tech.*, vol. MTT-31, no. 2, pp. 107–121, Feb 1983.

[14] J. S. Townsend, " sl The Theory of Ionisation of Gases by Collision," London: Constable, 1910.

[15] Z. J. Csendes, P. Silvester, "Numerical Solution of Dielectric Loaded Waveguides: I-Finite-Element Analysis," *IEEE Trans. Microwave Theory Tech.*, vol. MTT-18, pp. 1124–1131, Dec 1970.

[16] A. K. Sharma, G. I. Costache and W. J. R. Hoefer, "Cutoff in Fin-Lines Evaluated with the Spectral Domain Technique and with the Finite Element Method," *1981 IEEE AP-Symposium Digest*, pp. 308–311, June 16-19, 1981, L. A., California.

[17] F. Llewellyn-Jones, "*Ionization and Breakdown in Gases*," London: Methuen & Co. Ltd., New York: John Wiley & Sons Inc., 1957.

[18] A. D. MacDonald, "*Microwave Breakdown In Gases*," John Wiley & Sons, New York, 1966.

[19] M. R. Herlin and S. C. Brown, *Phys. Rev.74*, pp. 291,910, 1948.

[20] H. Margenan, *Phys. Rev.60*, pp. 508, 1946.

[21] Y. A. Lupan, A. A. Krasutskii, and S. V. Zakrevskii, "Microwave Breakdown Field in Air," *Sov. Phys. Tech. Phys. 23(6)*, pp. 649–650, June 1978.

[22] C. A. Brebbia, J. C. F. Telles and L. C. Wrobel, "*Boundary Element Techniques*," Springer-Verlag, Berlin Heidelberg NewYork Tokyo, 1984.

[23] A. Wexler, "Computation of electromagnetic fields," *IEEE Trans. Microwave Theory Tech.*, vol. MTT-17, pp. 416–439, Aug 1969.

[24] B. H. McDonald, M. Friedman and A. Wexler, "Variational solution of integral equations," *IEEE Trans. Microwave Theory Tech.*, vol. MTT-22, no. 3, pp. 237–248, March 1974.

[25] A. D. MacDonald, D. U. Gaskell and H. N. Gitterman, *Phys. Rev.130*, pp. 1841, 1936.

[26] F. Kossel and K. Kreds, *Z. Phys. Rev.139*, pp. 189, 1954.

[27] L. C. Shen and J. A. Kong, "*Applied Electromagnetism*, " PWS Engineering, Boston, Massachusetts, 1983.

[28] J. Daffe and R. G. Olsen, "An integral equation technique for solving rotationally symmetric electrostatic problems in conducting and dielectric material," *IEEE Trans. Power Apparatus Systems*, vol. PAS-98, no. 5, pp. 1609-1615, Sept, Oct 1979.

[29] P. K. Banerjee, R. Butterfield, "*Developments in Boundary Element Methods-1*," Applied Science Publishers Ltd., London, 1979.

[30] M. M. Ney, "Method of Moments as Applied to Electromagnetic Problems," *IEEE Trans. Microwave Theory Tech.*, vol. MTT-33, no. 10, Oct 1985.

[31] B. Lax, W. P. Allis and S. C. Brown, *Joul. Appl. Phys. Rev.21*, pp. 1297, 1950.